ALMA MATER STUDIORUM - UNIVERSITÀ DI BOLOGNA

SCUOLA DI INGEGNERIA

DIPARTIMENTO di
INGEGNERIA DELL'ENERGIA ELETTRICA E DELL'INFORMAZIONE
"Guglielmo Marconi"
DEI

CORSO DI LAUREA MAGISTRALE IN
Telecommunications Engineering

TESI DI LAUREA
in
Spacecraft Orbital Dynamics and Control

AUTONOMOUS DEEP SPACE SPACECRAFT ORBIT DETERMINATION VIA ONE-WAY UPLINK RANGING OBSERVABLES

CANDIDATO   RELATORE

Giacomo Paialunga   *Chiar.mo Prof. Marco Zannoni*

CORRELATORI

Prof. Paolo Tortora
Dr. Edoardo Gramigna

Anno Accademico
2022/2023

Sessione
II

A mio nonno Mario, a cui devo chi sono oggi.

Abstract

Most of space missions rely on measuring two-way range and Doppler observables, which involves timing how long it takes for a radio signal to travel from a ground station to the spacecraft and back. However, this type of navigation becomes less effective as the spacecraft moves further away from Earth, causing significative delays in signal propagation. In this thesis we try to verify if it is possible to enable autonomous spacecraft navigation through a time transfer link in the microwave domain between a ground station, equipped with its highly stable clock, and the spacecraft, outfitted instead with a clock characterised by a lower temporal and frequency stability. This time transfer implies a series of synchronisation windows, at the end of which the spacecraft will show the same time reference as its on-ground counterpart. This type of one-way navigation is crucial for all those critical operations when the signal from Earth would take too long to reach the spacecraft, especially for those space vehicles which travel towards very remote planets. In fact, in this novel paradigm, the ground control can let the spacecraft move along its designed trajectory without taking actions unless some unpredicted problem arises.

Table of contents

List of Figures

Chapter 1: Scientific Background

1.1. The meaning and benefits of space exploration

Deep space embodies the ultimate frontier of human imagination, a vast and mysterious unknown which has captured our curiosity since the dawn of time. As technological improvements have arisen over the decades, human beings have been able to progressively investigate and learn more and more about the cosmos. Humanity begins its journey on this planet in Africa but, over thousands of years, our ancestors migrated all over the continent and out of it. They built boats and they travelled incredibly long distances, heading toward the shores of lands they could not have known were there. A question can be raised immediately: "Why did they face so many dangers?". Probably for the same reason we turn our gaze to the night sky and wonder: "What is up there? Could we go there?". This is something human beings have done for centuries. Humans are driven to push the boundaries of science and technology always a step forward and, afterwards, push them further, providing benefits to our society and our species. Space exploration allows us to address those weighty questions about our place in the Universe and the history of our solar system. This leads to the advancement of technology, the establishment of new industries and the promotion of peaceful relationships with other nations.

Someone might ask the question, "What are the tangible benefits of space exploration for us here on Earth?" It is one that all those people involved in the space sector answer nearly every day. The products and outcomes of space exploration touch lives in several ways, mostly unknown to people. In this sense, we can cite a few of them:

- Health

  Medicine is a huge beneficiary of space exploration techniques. For example, anyone who underwent a digital X-ray, a mammogram or a CAT scan, could benefit from technologies first developed for use in space. In addition, one of the most promising sectors is osteoporosis research, a condition which determines a loss of bone mass and affects not only the elderly but also astronauts on the International Space Station (ISS). As a consequence, there is plenty of opportunity to trial new treatments in space.

- Innovative discoveries

  Many innovations which have become a part of our daily lives derive from space research, from the thermal space blanket used by marathon runners at the conclusion of races to the portable vacuum cleaners that we commonly find in our homes.

- New raw materials

  The possibility of extracting raw materials from asteroids or even from our "closest neighbour" the Moon will not only represent a fast track to turn space material into ready cash but it will also provide brand new technological possibilities. For example, the Moon is rich in helium-3 which is a very rare isotope here on Earth and it can be mostly used for nuclear fusion.

- Worldwide communication and monitoring

  Almost anyone on Earth has a mobile phone but what people do not know is that those phones they hold in their hands use processes and materials developed for space-age communication. Those devices can "talk" to GPS satellites orbiting our planet, without which we could not know our location or the route to reach a desired destination. Moreover, there are satellites which take pictures of the planet, helping meteorologists to predict weather and track hurricanes. In addition, there are satellites monitoring the Sun and they are in charge of warning scientists, astronauts or satellite operators of potential space weather storms that could impact the communications infrastructure. Finally, various satellites play a crucial role in capturing images of other planets, black holes, dark matter or faraway galaxies, allowing us to gain a better understanding of the cosmos.

- Space colonisation

  Human beings have caused enough damage to our planet. Therefore, if we want the human race to survive, we will need to search for and colonise a new world. Survival is clearly the primary motivation for humans to become a multi-planetary species. Although hypothetical mass extinction events like irreversible climate change, asteroid impacts or nuclear war might be unpleasant to think about, our technologies have advanced and our search has already begun. How close or how far are we to establish ourselves on Mars?

According to the Harward Business Review (Sarang M., Weinzierl M., 2021), the term "space economy" covers the "goods and services produced in space for use in space, such as mining the moon or asteroids for material". The OECD[1] defines it as any activity that involves "exploring, researching, understanding, managing, and utilising space". In whatsoever terms it is defined, this space economy is not only growing by itself but it is a fundamental enabler of growth in many other sectors of society and the economy.

1.2. Spacecraft navigation

The spacecraft navigation system represents one of the main technological components of deep space exploration missions. In the space environment, everything is moving, not only the spacecraft itself but also the destination planet or moon. For example, a spacecraft on the launch pad is orbiting the Sun together with the Earth, while there are spacecraft orbiting moons or other bodies, which, in turn, orbit the Sun or there are spacecraft which reach a sufficient velocity to follow hyperbolic paths with respect to the Sun, orbiting the centre of our galaxy as the Sun itself. This is a fundamental concept to keep in mind when planning and executing a space mission, since there are no fixed positions in this context and navigating a spacecraft is not as easy as going from point A to point B. To make a comparison, the navigation of a spacecraft might be associated with sailing a ship in the open sea or driving a car along a particularly arduous path. Simply put, spacecraft navigation involves the determination of the spacecraft's position and its maintenance on the desired trajectory towards a specific destination. However, space navigators must face several challenges in order to accomplish their objectives. First of all, the distances encountered are enormous and this aspect does not ease the communication with the spacecraft, since the signal sent from the ground takes a significantly large amount of time to reach the spacecraft itself. Moreover, the level of power available on board for radio communication with Earth is limited because, as long as the space vehicle travels further and further away from our planet, it is not capable of generating considerable power through solar panels. Finally, gravity has a role in affecting the trajectory of a spacecraft, so these gravitational perturbations must be taken into account to properly design the mission.

---

[1] OECD, 2012.

1.2.1. Earth-based navigation overview

Spacecraft navigation includes three main aspects:

- The design of a reference trajectory which describes the planned flight path of the spacecraft.
- Keeping track of the actual spacecraft position while the mission is in flight.
- Performing manoeuvres to bring the spacecraft back to the reference trajectory when it has drifted (Doody D., 2022).

The spacecraft always tends to drift away from its nominal orbit due to the various disturbances it encounters during its voyage in space. As a matter of fact, even tiny disturbances, like the Sun's pressure, can add up over time and push the spacecraft off course. During the reference trajectory design phase, the team tries to consider all these disturbances but it is not possible to entirely account for the randomness of these events. Therefore, the orbit determination process is an iterative procedure involving the so-called radiometric observables (i.e., measurements), which, in general, are obtained from the amplitude and the phase of an electromagnetic wave which establishes a radio link between the spacecraft and the Earth itself. In this sense, the expected values of these tracking observables are computed, with the help of nominal values for the trajectory and exact models. These calculated observables are compared with the actual values obtained from the tracking system to shape the data residuals[2]. If we had a perfect knowledge of the trajectory and the models, the residuals would be Gaussian distributed because of uncorrelated measurement errors. Nevertheless, the intrinsic errors present inside the models of the tracking observables and the trajectory insert signatures in the residuals, enabling an adjustment of the model parameters. This adjustment is performed through a weighted linear least-squares estimation, a procedure where the optimal solution is represented by the set of parameter values which minimizes the weighted sum of squares of residuals. This procedure is iterative because the steps must be repeated, each time using the latest estimates of the parameter values until the solution converges (Border J. S., Thornton C. L., 2000).

---

[2] Residuals are estimates of experimental error obtained by subtracting the observed responses from the predicted responses, representing a key component of all statistical modelling.
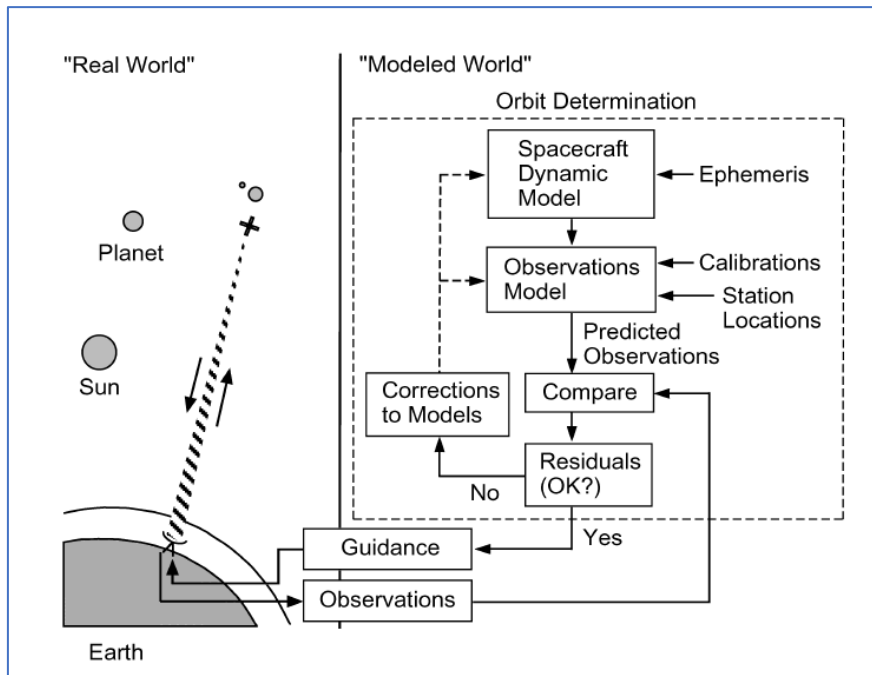
Figure 1. A scheme representing the navigation process.
Credit: NASA/Jet Propulsion Laboratory-California Institute of Technology.

Once a good estimate for the current location of the spacecraft has been determined, it is necessary to evaluate how far the spacecraft has drifted from the reference trajectory, in such a way that guidance algorithms are executed to compute any required retargeting manoeuvres. Upon completion of these calculations, a ΔV vector is derived, showing the direction and magnitude of the adjustment in the spacecraft velocity essential for the spacecraft to resume its intended course. This clearly outlines the spacecraft's pointing requisites and the corresponding rocket-engine or thruster operations. A set of instructions is prepared and subsequently uplinked to the spacecraft to execute the manoeuvre. It is plausible that the thrusters were not accurately aligned or the engine was switched off a bit too late and, consequently, it is required to collect additional tracking data to verify the manoeuvre's success. After a manoeuvre has been performed, the cycle repeats; this iterative process of orbit determination and flight path control persists throughout the mission, as the spacecraft consistently strays from its intended trajectory and must be guided back. In spaceflight, specific ΔV manoeuvres are classified as "deterministic". This indicates that their execution and the expected ΔV value are predetermined to uphold the reference trajectory. In contrast, other ΔV manoeuvres are labelled as "stochastic", implying that their execution and resulting ΔV value cannot be accurately forecasted due to inherent uncertainties, such as those associated with gravity-assist flybys. Finally, it is crucial to note that a spacecraft's ability to alter its velocity is restricted by the amount of propellant it can hold. As such, when designing a spacecraft and selecting a launch vehicle, it's critical to

ensure that it can accommodate enough propellant to execute any necessary manoeuvres. Simply put, the spacecraft must possess adequate ΔV capability to satisfy all its operational needs (Doody D., 2022).

1.2.2. Range and Doppler observables

A fundamental step in the navigation process is the measurement from Earth of some mathematical quantities, denoted as observables, which are characteristic of the motion of the spacecraft. Specifically, these meaningful observables[3] are:

- The spacecraft's range, that is to say, its distance from Earth.
- The component of the spacecraft velocity directly toward or away from Earth, denoted as Doppler since it is obtained from the extraction of the Doppler shift experienced by the signal exchanged between the ground station and the spacecraft itself.
- The spacecraft's position in Earth's sky.

The measurements of Doppler and range offer a very good understanding of how space vehicles move in space. If a collection of range and Doppler observables is gathered from multiple ground stations situated at different locations on the Earth's surface over a specific timeframe, it can provide a restricted number of trajectories. This approach enables us to develop an updated trajectory model which aligns with the measurements, ultimately providing a solution to the orbit determination problem. With the aim of obtaining the spacecraft's range according to a two-way link architecture, a certain ground station generates a uniquely coded ranging signal which is then phase-modulated onto the transmitted carrier wave. The receiver equipment generates a reference signal coherent with the uplink carrier employing a phase-locked loop. Afterwards, this reference signal is implied in the demodulation of the ranging signal, which is low-pass filtered and phase-modulated onto the downlink carrier at a different frequency. The same process repeats at the receiving ground station as well, where another phase-locked loop allows to demodulate the downlink signal by generating a new reference signal coherent with the received signal. At this point, when the received code is compared to a transmitted code model, the round-trip transmit time is determined. The slant range can be indeed approximately

---

[3] These measurements are based on Earth and, for this reason, they rely on precise knowledge of Earth's orbital parameters and inherent motions, with the result that the measurements make sense in a heliocentric (Sun-centred) reference system.

expressed in relation to the one-way transmit time of the signal denoted as τ_g in the following way:

$$\rho = \tau_g c$$

where c represents the speed of light. For a two-way signal, the range observable can be written as:

$$\rho = \frac{1}{2}(t_3 - t_1)\,c$$

where t_1 is the transmission time at the ground station, t_2 is the receiving time at the spacecraft, t_3 is the receiving time at the ground station. An example of this type of scheme can be seen in the following Figure 2.
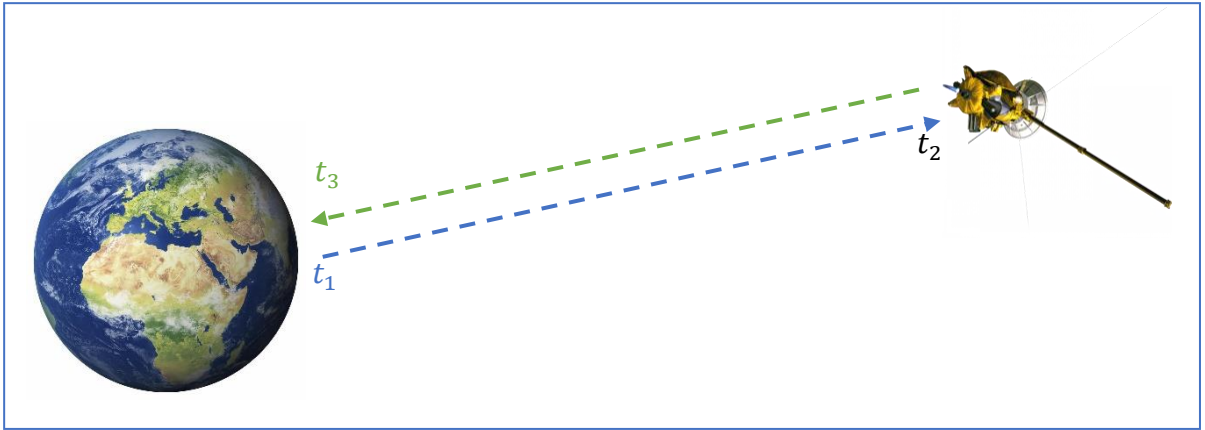
Figure 2. An example of a two-way link.

Furthermore, it is possible to write an approximate expression for the received frequency at an Earth-based antenna as:

$$f_R = \left(1 - \frac{\dot{\rho}}{c}\right) f_T$$

where f_T is the frequency transmitted by the spacecraft and $\dot{\rho}$ is the spacecraft's instantaneous slant range rate. In particular, the term $\left(\frac{\dot{\rho}}{c}\right) f_T$ is the so-called Doppler shift. As a consequence, Doppler data give us insight into the spacecraft range rate and, thus, obtained by differentiating the received reference signal with the station frequency reference. A simplified representation of the Doppler extraction process is depicted in Figure 3. The difference between the transmitted

13

and the received carrier frequencies provides the Doppler frequency. Afterwards, a cycle counter determines the phase change of this Doppler tone, resulting in a measure of the range change during the count time interval (Border J. S., Thornton C. L., 2000).
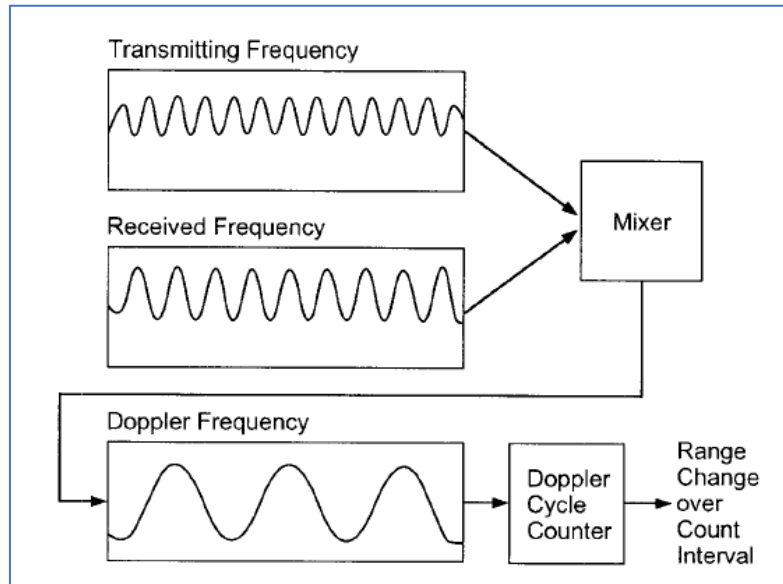
Figure 3. A scheme representing the Doppler extraction process.
Credit: NASA/Jet Propulsion Laboratory-California Institute of Technology.

1.3. State-of-the-art of one-way navigation

As previously highlighted, one of the fundamental technological components in the context of deep space exploration missions is represented by the spacecraft's navigation system. At present, most of these missions are based on two-way range and Doppler observables, measured starting from the time taken by a radio signal to complete its round trip from the ground station to the spacecraft. The problem with this type of measurement clearly emerges when the spacecraft progressively increases its distance from the Earth, heading towards deep space. As the spacecraft moves away, there is an increase in the propagation time of the two-way signal, making this type of navigation inadequate for all those occasions in which timely decisions are required regarding trajectory, attitude and anything else, in addition to situations in which a possible crew requests real-time information regarding their position. For example, as a spacecraft nears its destination planet, the ground station might not have enough time to establish contact with the spacecraft before it enters the orbit injection or descent phase. To address this issue, collecting and processing one-way radiometric signals from a single transmitting station on board is ideal. This will enable autonomous real-time navigation, which

is crucial for executing time-critical operations such as planetary landings or planetary flybys. In these situations, signal delays can prevent ground interaction, making autonomous navigation a necessity (Bian L., Lei W., Meng Y., Wang G., Wang Y., Yan T., 2017).

1.3.1. The Deep Space Atomic Clock demonstration

The advent of NASA's Deep Space Atomic Clock (DSAC) has made it possible to reliably and accurately collect one-way radiometric observables sent from a beacon, such as a DSN antenna or another spacecraft. As previously mentioned, spacecraft which venture into deep space rely on communication with ground stations to ascertain where they are and where they are going. The exchange of two-way signals between the spacecraft and the ground station is therefore essential to be able to precisely calculate the trajectory of the spacecraft itself, using large atomic clocks on the ground to record the times of those signals. However, when dealing with rovers and robots scanning and studying the Martian soil, or even vehicles headed towards far-off destinations such as Jupiter, Saturn or Uranus, the time interval taken by the signals to cover the entire round-trip route can quickly reach tens of minutes or even hours. These ground-based atomic clocks have served as the gold standard for precise timekeeping since the 1950s. At the same time, they are the cornerstone of deep-space navigation for most space missions because of their fundamental role in navigation measurements. These clocks measure very stable and precise frequencies of light emitted by specific atoms, using them to regulate the time more traditional mechanical clocks keep. Despite this phenomenal accuracy, their size, power consumption and sensitivity to environmental changes make them impractical for use in space. In addition, they are still susceptible to instabilities that can cause slight discrepancies, or "offsets", in the displayed time compared to actual time. If these offsets are not corrected, they can accumulate and lead to significant positioning errors. In situations such as space travel, even a fraction of a second can be the difference between a successful arrival on a planet or missing it entirely. Consequently, the clocks must be toughened and miniaturized to make them suitable for space exploration (O'Neill I. J., 2021). Indeed, if spacecraft were equipped with atomic clocks themselves, they could calculate their own position and direction, provided the clocks were highly stable.

Figure 4. An illustration showing NASA's Deep Space Atomic Clock operating aboard the General Atomics Orbital Test Bed satellite.
Credit: General Atomics Electromagnetic Systems.

The DSAC has worked to give these deep space explorers greater autonomy during navigation. Built by NASA's Jet Propulsion Laboratory, the DSAC is an ultra-precise, mercury-ion atomic clock encased in a small box which measures about 25 centimetres on each side. It was a vital technology demonstration intended to achieve pioneering advancements, enduring the stresses of launch and the severe, high-radiation environment of outer space without degrading its timekeeping performance. The DSAC uses the property of mercury ions' hyperfine transition frequency at 40.50 GHz to regulate the frequency output of a quartz oscillator and maintain it to a near-constant value. In order to perform this operation, DSAC confines the mercury ions with electric fields in a trap and safeguards them through the application of magnetic fields and shielding. The result is a remarkably stable environment for precise measurement of the hyperfine transition, minimizing sensitivity to temperature and magnetic fluctuations. Furthermore, the DSAC technology has almost no expendables, enabling the development of a clock suitable for extended space missions (Jet Propulsion Laboratory, 2021). Initially launched on 25th June 2019 on a SpaceX Falcon Heavy[4] rocket as part of the Department of Defense's Space Test Program-2 (STP-2) for a one-year primary mission in Earth's orbit, the clock's

---

[4] Falcon Heavy is a two-stage, heavy-lift launch vehicle composed of three reusable Falcon 9 nine-engine cores. As one of the world's most powerful operational rockets, Falcon Heavy can lift nearly 64 metric tons to orbit. SpaceX first launched the Falcon Heavy vehicle in February 2018.

exceptional stability prompted NASA to extend the mission to gather additional data. It was ultimately powered off on 18th September 2021. The DSAC has surpassed all expectations and demonstrated outstanding reliability as an atomic clock for space applications with a stability (including drift) at a day of $\sim 3 \times 10^{-15}$ and a long-term linear frequency drift below 3×10^{-16} at a day. In the context of an analogue deep space navigation experiment, the one-way radiometric tracking obtained by using the clock was comparable to that of its two-way counterpart for orbit determination, thus confirming its potential as a navigation tool in the future (Ely T. et al., 2022). The next step is embodied by the Deep Space Atomic Clock-2, an upgraded model of the cutting-edge DSAC, which will be developed thanks to the data collected by the instrument itself. The new clock will travel to Venus aboard NASA's Venus Emissivity, Radio Science, InSAR, Topography and Spectroscopy (VERITAS[5]) spacecraft, set to launch by 2028. Similar to its predecessor, the new space clock is a technology demonstration, designed to improve meaning its goal is to advance in-space capabilities by developing new tools, hardware and software which are not yet available (Cofield C., 2021). However, the DSAC-2 will be more compact, energy-efficient and tailored to support a multi-year mission like VERITAS.
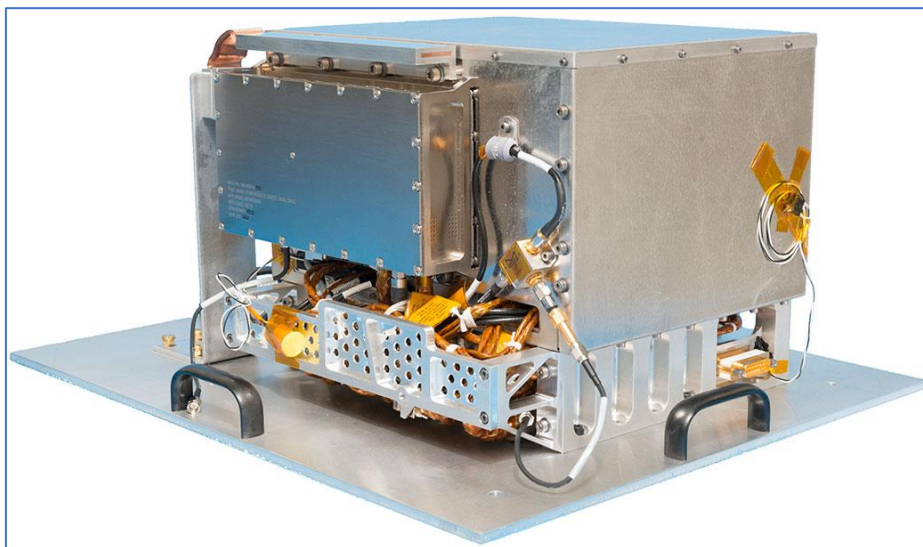
Figure 5. NASA's Deep Space Atomic Clock hardware unit.
Credit: NASA/Jet Propulsion Laboratory-California Institute of Technology.

---

[5] VERITAS will study the surface and interior of Venus with a powerful new generation of scientific tools, representing the first NASA mission to return there since the 1990s. The mission was selected for flight in 2021 as part of NASA's Discovery program. NASA's Jet Propulsion Laboratory is responsible for mission management, operations and navigation.
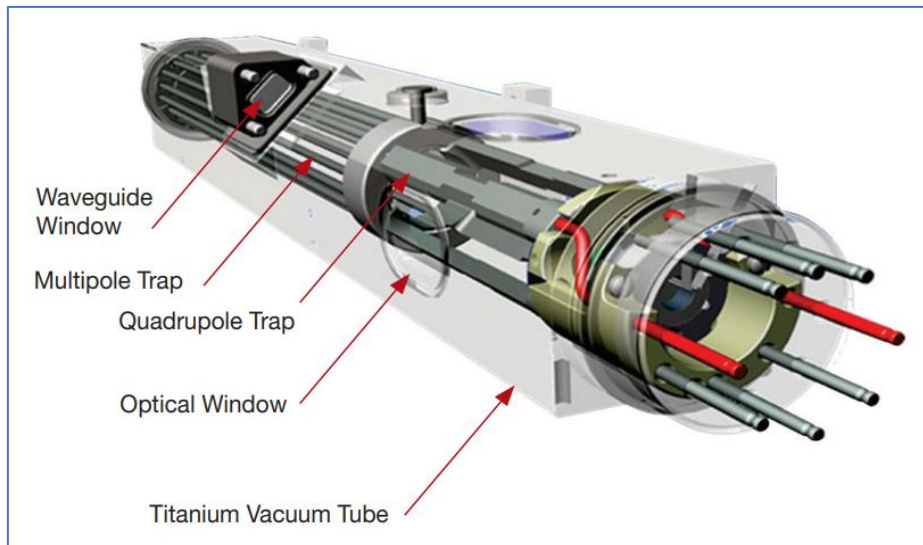
Figure 6. A drawing of the DSAC mercury-ion trap showing the traps and the titanium vacuum tube that confines the ions. The quadrupole trap is where the hyperfine transition is optically measured and the multipole trap is where the ions are "interrogated" by a microwave signal via a waveguide from the quartz oscillator. Credit: NASA/Jet Propulsion Laboratory.
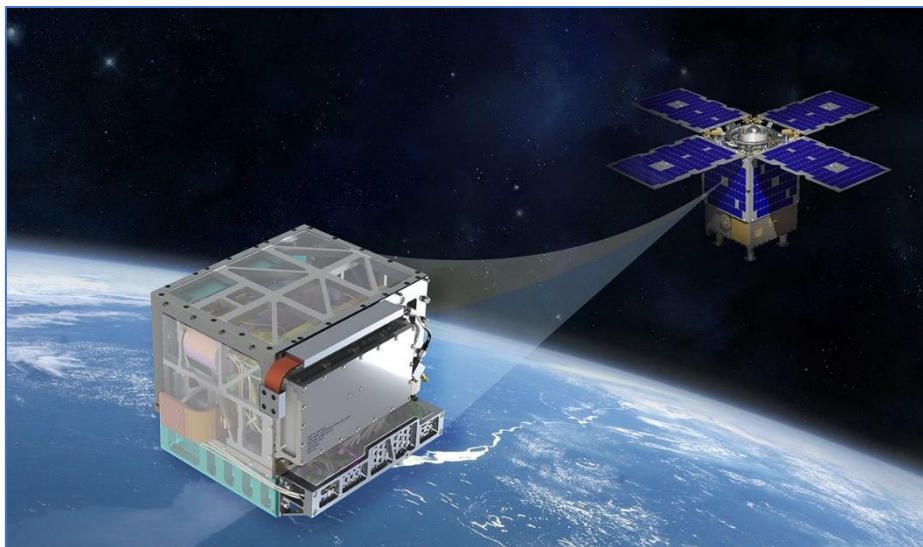
Figure 7. An illustration which shows NASA's Deep Space Atomic Clock demonstration and the General Atomics Orbital Test Bed spacecraft that hosts it. Credit: NASA.

The DSAC marks a significant shift towards a one-way radiometric tracking architecture, unlike the two-way architecture provided nowadays by NASA's Deep Space Network[6] (DSN). This

---

[6] The Deep Space Network (DSN) is NASA's international array of giant radio antennas which support interplanetary spacecraft missions, plus a few that orbit Earth. Additionally, the DSN also provides radar and radio astronomy observations, deepening our understanding of the solar system and the larger universe.

transition holds the promise of not only increasing the amount of tracking data but also the quality of that data as well, paving the way for autonomous radio navigation. The main advantages of DSAC are listed below.

- Augmented tracking data quantity

The DSN can support multiple downlinks on a single antenna (Multiple Spacecraft Per Aperture or MSPA[7]) but, regrettably, only one uplink signal can be supported concurrently. In case multiple spacecraft are at the same time in view of a DSN antenna, they must share time utilizing the uplink signal, ultimately curtailing the amount of two-way Doppler tracking data. On the other hand, a spacecraft equipped with DSAC can supply one-way downlink radiometric tracking on a certain ground antenna throughout the entire spacecraft's visibility period at no tracking time cost to another spacecraft in view of the same antenna. In those scenarios in which the round-trip light time is significant, opting for DSAC-based one-way radio tracking can prove more effective than two-way tracking. This is because one-way tracking can make use of the entire view period of an antenna, whereas two-way tracking is constrained by the round-trip light time. Consider the Cassini[8] mission, for instance. The view periods of Saturn's northern hemisphere at Goldstone and Madrid antennas were in the order of 11 hours but, with a round-trip light time of 2-3 hours, the available two-way tracking window was reduced to just 8-9 hours. On the contrary, a one-way tracking pass based on DSAC could leverage the full 11 hours, leading to an increase in usable data from 19% to 27%. Further, when spacecraft are in the outer regions of the solar system, a three-way architecture is needed. This implies the use of two distinct DSN stations to transmit the tracking signal to the spacecraft and receive it upon its return. Obviously, this is due to the huge distance between the Earth and the spacecraft which leads to a too large round-trip light time. With the help of DSAC, only one DSN antenna is required to mould the one-way measurement, freeing up the other antenna to support another mission.

---

[7] Multiple Spacecraft Per Aperture (MSPA) is a special configuration wherein multiple receivers are connected to a single DSN antenna permitting the simultaneous reception of signals from two or more spacecraft, provided that they are all within the Earth station's beamwidth. As a consequence, MSPA makes more efficient use of DSN facilities by enabling simultaneous data capture from several space vehicles.

[8] Cassini-Huygens was a joint mission of NASA, the European Space Agency (ESA) and the Italian Space Agency. Cassini was launched in 1997 along with ESA's Huygens probe. After studying Jupiter for six months in 2000, it reached Saturn in 2004 and began a series of flybys of Saturn's moons. That same year the Huygens probe was released onto Saturn's moon Titan to study its atmosphere and surface composition.

- Enhanced tracking data quality

Radio signals can be strongly impacted by the perturbations caused by solar plasma, especially for spacecraft travelling at low Sun-Earth-Probe (SEP) angles. Since this plasma disturbance is inversely proportional to the square of the transmission frequency, two-way Ka-band tracking at 32 GHz is capable of reducing the signal noise by a factor of approximately 15 compared to X-band tracking at 8.4 GHz and by roughly 10 times compared to an X-band uplink/Ka-band downlink combination. While the Goldstone DSN site supports both Ka-band uplink and downlink, the Canberra and Madrid DSN sites only support Ka-band on the downlink. However, spacecraft equipped with DSAC can be tracked solely on the Ka-band downlink, regardless of the DSN site, reducing measurement noise by an order of magnitude compared to an X-band uplink/Ka-band downlink. Provided that the solar plasma disturbance can be reduced at Ka-band, the main constituent of the Doppler measurement noise is represented by the Earth's tropospheric signal delay. In particular, this delay includes two contributions: the dry part, constituting 80% and the remaining wet part. While the dry troposphere error is typically well-calibrated, removing the wet error can be challenging in certain situations. Failure to calibrate properly could result in a three-fold increase in Ka-band Doppler noise in the zenith direction. Nevertheless, in a DSAC one-way downlink, it is possible to avoid adverse weather conditions at a ground location if all Ka-band receivers are able to receive the signal, thereby mitigating signal degradation.

- Spacecraft design

When employing an uplink one-way approach for tracking, the needed signal power is diminished. In this way, through the utilisation of DSAC, the spacecraft can operate with lower gain antennas which offer a more omnidirectional coverage. Consequently, a greater amount of tracking data can be recorded during a wide range of operations than with the two-way counterpart.

- Autonomous deep space navigation

A spacecraft outfitted with DSAC tracking a one-way uplink transmission through its onboard receiver is capable of autonomously navigating in deep space. However, this autonomy can be fully achieved by implementing a navigation system which combines the DSAC-enabled one-way uplink radiometric tracking system with optical tracking thanks to a camera. This

integration would merge the strengths of radio navigation for determining absolute location in deep space and planetary orbits with the target relative navigation provided by the optical system. Therefore, this effective association would prove highly beneficial for robotic missions where ground-in-the-loop operations are not feasible, such as deep space encounters, planetary capture, real-time orbital operations and so on and so forth. In addition, it would facilitate crewed exploration missions in deep space which require operations without ground support (Ely T., Seubert J., 2015).

Chapter 2: Study on potential one-way uplink navigation

As previously discussed, one-way navigation represents a promising prospect for future deep-space missions. The real turning point is the capacity to gather and process one-way observables directly on board, empowering the autonomous navigation of the spacecraft. In particular, this type of one-way navigation represents an indispensable element for all those operations which can be defined as "time critical", such as planetary landings or the execution of planetary flybys, when the signal from Earth would take too long to reach the spacecraft, making it impossible for Earth control to effectively interact with it. This is particularly helpful for those space vehicles headed towards very distant targets, such as Jupiter, Saturn or Uranus because we do not need to perform orbit determination over an arc period of several years but the spacecraft is capable of navigating through space by itself and the control team intervenes only in case of anomalies. This thesis has the objective of carrying out a preliminary study about the feasibility of autonomous spacecraft navigation based on one-way range and Doppler observables via a microwave link between the ground station and the spacecraft. The study begins with the analysis of the Atomic Clock Ensemble in Space (ACES) mission, a fundamental physics mission of the European Space Agency (ESA). ACES relies on a high-performance clock onboard the International Space Station, a network of high-performance clocks on the ground and a dedicated two-way microwave link, enabling space-to-ground and ground-to-ground clock comparisons. After the analysis of ACES mathematical model, the relative equations have been handled in order to develop a new theoretical framework which can fit a different scenario: a one-way uplink architecture. Finally, a simplified scheme of the same one-way uplink architecture has been built by means of MATLAB[9] programming language, which is based on matrix calculus and allows to couple the opportunity to utilise advanced numerical tools with the graphical representation of the obtained outputs. The aim of the simulated scheme is to test the aforementioned equations and obtain proper preliminary results to examine the practicability of such one-way uplink navigation. This will pave the way for future works to further explore this topic.

---

[9] For more information, see <https://it.mathworks.com/products/matlab.html>.

2.1. The ACES mission

The basis of General Relativity and, in general, of all metric theories of gravitation is the Einstein Equivalence Principle (EEP) (Will C.M., 2014) and, consequently, it calls for broad experimental validation. While the different aspects of the EEP, such as the Universality of Free Fall[10] (UFF) and the gravitational redshift of clocks[11], are related, their relationship cannot be predetermined and, therefore, they need to be tested independently. In particular, the gravitational redshift of clocks was best tested in the Gravity Probe A experiment. This test compared a hydrogen maser aboard a rocket on a parabolic trajectory to a hydrogen maser on the ground via a two-way microwave link. One of the main scientific objectives of the ACES/PHARAO mission is to improve these results by roughly two orders of magnitude.

The ACES/PHARAO mission is an international metrological space mission led by the European Space Agency (ESA) in collaboration with the French Space Agency (Centre National d' Études Spatiales, CNES). It aims at building a highly stable and accurate time scale on board the International Space Station (ISS) using a unique cold-atom space clock (PHARAO) developed by CNES in collaboration with LNE-SYRTE, together with a space hydrogen maser (SHM). Moreover, ACES will be outfitted with microwave (MWL) and optical (European Laser Timing, ELT) links which will allow frequency and time comparisons between the onboard time scale and time scales on the ground. As the ISS clock moves through the Earth's gravity potential at orbital speed, the timescale developed onboard will be able to track the clock's proper time. This will progressively accumulate a time difference with respect to its counterpart on the Earth's surface. Thanks to the monitoring of the clock desynchronisation, it will be possible to test the predictions of General relativity. Clearly, these tests will be affected by the noise introduced by the clocks themselves and the link between them (Meynadier F. et al., 2018). Provided that τ denotes the integration time, the clock ensemble relative frequency stability expressed in Allan deviation, ADEV (Allan D. W., 1966), should be better than $\sigma_y = 10^{-13} \cdot \tau^{-1/2}$, which corresponds to 3×10^{-16} after one day of integration. On the other hand, time deviation (TDEV) should be better than $2.1 \times 10^{-14} \cdot \tau^{1/2}$, which corresponds to $12 \, ps$ after one day of integration. The fractional frequency uncertainty of the clock ensemble should be around 10^{-16}. As the expected gravitational frequency shift between ground and space

---

[10] The universality of free fall (UFF) refers to any objects which are subjected to the same acceleration during free fall regardless of their classical or quantum nature. This concept represents a foundation of modern physics.
[11] Einstein's theory of general relativity predicts that a clock at a higher gravitational potential will tick faster than another identical clock at a lower potential. This effect is known as gravitational redshift.

clocks for an ISS altitude of 400 km is around 4×10^{-11}, this is coherent with a measurement of the gravitational redshift in the order of 3×10^{-6} (Delva P., Laurent P., Le Poncin-Lafitte C., Meynadier F., Wolf P., 2012 and Meynadier F. et al., 2018). Unfortunately, the ACES program has recently suffered from major delays due to the challenges encountered in the development and testing of the active hydrogen maser and the time transfer microwave system. Moreover, the COVID-19 pandemic has further exacerbated the situation but, thanks to the unwavering support from the worldwide scientific community, National Space Agencies and ESA, the ACES program has regained momentum and access to new resources. The revised schedule estimates that ACES will be ready for launch to the ISS in 2025 (ACES Workshop, 2022). The main scientific objectives of the mission are (Cacciapuoti L., Salomon C. et al., 2009 and 2015):

- To demonstrate the high performance of the atomic clock ensemble in the space environment and the possibility of achieving high stability on space-ground time and frequency transfer.

- To compare ground clocks at high resolution across the world by using the microwave link. In common view mode, the link stability should reach around $0.3\ ps$ after $300\ s$ of integration; in non-common view mode, the stability should be around $7\ ps$ after 1 day of integration.

- To conduct Equivalence Principle tests. The experiment will provide an unparalleled opportunity to test gravitational redshift, to carry out novel trials of Lorentz invariance and to search for possible variations of fundamental constants.

2.1.1. The ISS clock ensemble

The clock ensemble aboard the ISS is made up of two clocks, PHARAO and SHM (Laurent P. et al., 2006). Specifically, PHARAO is a laser-cooled Caesium clock, where the main sources of frequency shifts are the collisions between cold atoms and the first-order Doppler effect. A short-term servo loop steers PHARAO's local oscillator towards the clock signal of SHM with a typical time constant of a few seconds while a long-term servo loop corrects SHM's 100 MHz clock signal with a time constant of a few hundred seconds. The ACES clock signal is derived from both PHARAO and SHM signals, coupling the medium-term stability of the SHM and the long-term stability of PHARAO. As a result, the Allan deviation is limited by SHM's performance on medium time scales and by PHARAO's performance on long time scales for

an overall relative frequency stability, as previously mentioned, equal to roughly $10^{-13} \cdot \tau^{-1/2}$ and a time deviation of $12\,ps$ after one day of integration. The performance of the PHARAO/SHM clock ensemble sets the requirement for the performance of the MWL and the ELT.
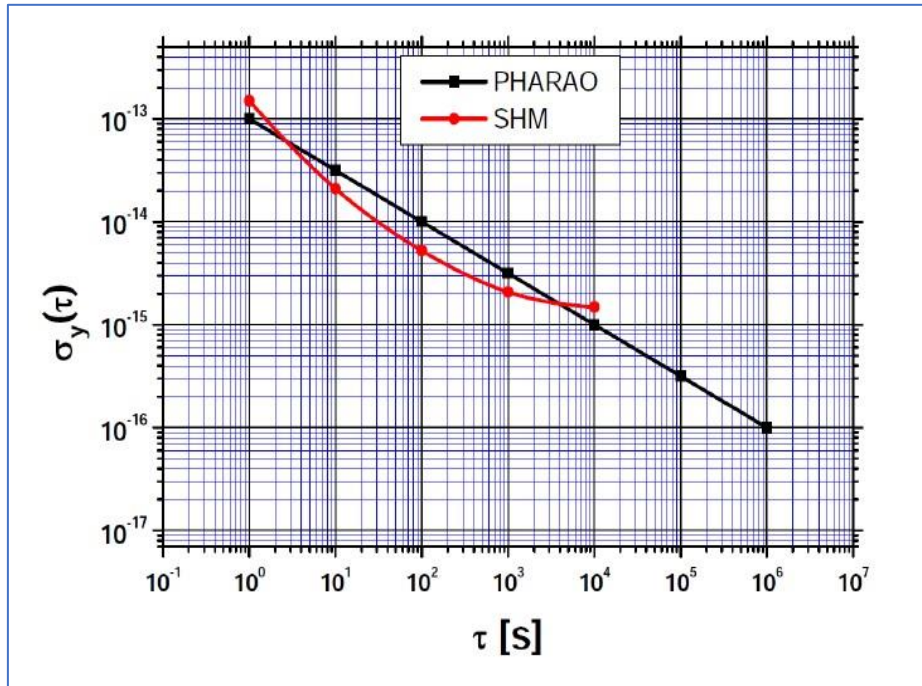

Figure 8. PHARAO and SHM expected performances expressed in Allan deviation.
Credit: Delva P., Laurent P., Le Poncin-Lafitte C., Meynadier F., Wolf P., 2012.
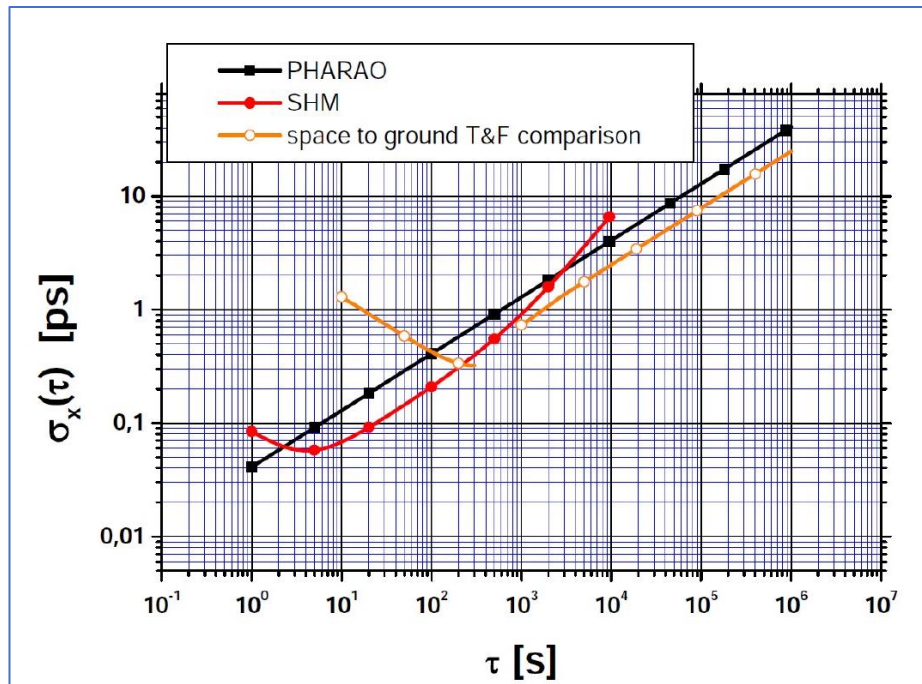
Figure 9. Performance objective of the ACES clocks and the ACES space-ground time
and frequency transfer expressed in time deviation.
Credit: Delva P., Laurent P., Le Poncin-Lafitte C., Meynadier F., Wolf P., 2012.

2.1.2. The microwave link

The space-ground time and frequency transfer[12] will be made possible by means of the microwave link (MWL). The MWL is composed of three signals at different frequencies: one Ku-band uplink at frequency $f_1 \cong 13.5\ GHz$ and two downlinks at $f_2 \cong 14.7\ GHz$ and $f_3 \cong 2.2\ GHz$ (Ku and S-band, respectively). A specific configuration of these three links is chosen, denoted as Λ configuration, since it minimises the error coming from the uncertainty on ISS orbitography. The f_1 frequency signal is emitted by the ground station at the coordinate time t_1 and received by the space station at t_2. The f_2 and f_3 frequency signals are emitted from the space station at t_3 and t_5 and received at the ground station at t_4 and t_6. The third frequency is added to measure the Slant Total Electron Content (STEC) in the ionosphere, which allows the correction of the ionospheric delay itself. In particular, the Λ configuration is achieved by setting $t_2 = t_3 = t_5$ (Duchayne L., Mercier F., Wolf P., 2009) and it is shown in Figure 10.
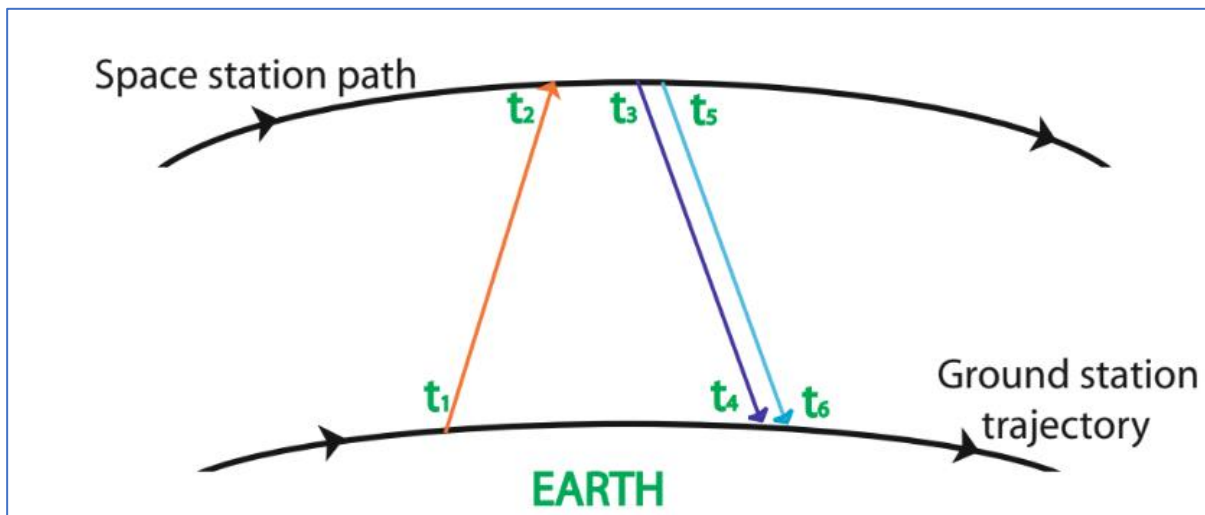
Figure 10. An illustration of the MWL principle.
Credit: Duchayne L., Mercier F., Wolf P., 2009

The MWL is characterized by its continuous emission. The type of signal involved is made up of a carrier modulated by a PRN (PseudoRandom Noise) sequence at 100 Mchip/s, obtained through a Gaussian white noise sampling process. The system measures the time interval between the received signal and the locally generated signal. It provides three measurements

---

[12] In particular, a time transfer represents the possibility of synchronising distant clocks, that is, determining the difference between the displayed times (desynchronisation) within a coordinated time reference system t. A frequency transfer is the ability to syntonise distant clocks, i.e., determine their difference in frequency within the same coordinated reference time t.

(or observables) by comparison of the code (one on board the ISS, the other two at the ground station) as well as three phase measurements of the carrier frequency. These six "carrier" and "code" observables are provided by the system at a sampling rate of $1\ Hz$. To better understand the nature of the MWL observables, it is possible to consider a piece of code generated by the ground clock at τ_p^g and received by the space clock at τ_a^s. The same piece of code is produced at the space clock at τ_p^s. A measurement of the MWL corresponds to the difference between the production and the arrival of the piece of code considered in the local time scale of the measurement (Duchayne L., 2008).

$$\Delta\tau^s(\tau_a^s) = \tau_p^s - \tau_a^s$$

Since the two clocks produce the same code, it is possible to express:

$$\Delta\tau^s(\tau_a^s) = \tau_p^g - \tau_a^s$$

Observables are similar to the ones of Global Navigation Satellite Systems (GNSS). The emitted electromagnetic signal is locked to the clock signal of the emitter and the time of arrival of this electromagnetic signal is compared to the clock signal generated by the receiver. Therefore, the basic one-way observable is a pseudo-time-of-flight[13] (PToF), which contains information about the signal's time-of-flight and the difference between the times given by the receiver and the emitter clock. The record of these observables is in charge of the ground and space modems, developed by TimeTech/Astrium for the ACES/PHARAO mission, which will be linked to the clocks and the antennas. Specifically, a PPS signal (one Pulse Per Second), a 12.5 PPS (one pulse every 80 ms, which is the measurement interval) and a periodic signal (either code at 100 MHz or carrier) are generated at both the emitter e and the receiver r. For instance, a PPS signal is sent at local time τ_{pps}^e of the emitter and is received at local time τ_{pps}^r of the receiver. In particular, τ_{pps}^r is recorded by the modem for each PPS. As shown in Figure 11, at the receiver side the 1 and 12.5 local PPS are generated, together with a local sine signal, denoted as the receiver's Local Oscillator and depicted in yellow. The mixing between the received periodic signal (depicted in blue) and the local oscillator generates a beat note (in green), which is filtered through a low-pass filter. Thanks to this filtering process, it is possible to extract the low frequency component of the beat note, whose frequency is around 195 kHz

---

[13] In GNSS it is more usual to talk about pseudo-ranges, which is the same as the PToF multiplied by c, the speed of light in vacuum.

for code and 729 kHz for carrier. At this point, the measurement phase takes place because, for each 80 ms interval, the receiver's device records the time of the first ascending zero-crossing of the filtered beat note signal, denoted as T_m where m is the number of the 80 ms sequence. Moreover, the modem counts the number of ascending zero-crossing n_m during sequence m. τ_{pps}^r, T_m, n_m and m represent the so-called TT observables and are recorded for code and carrier signals.
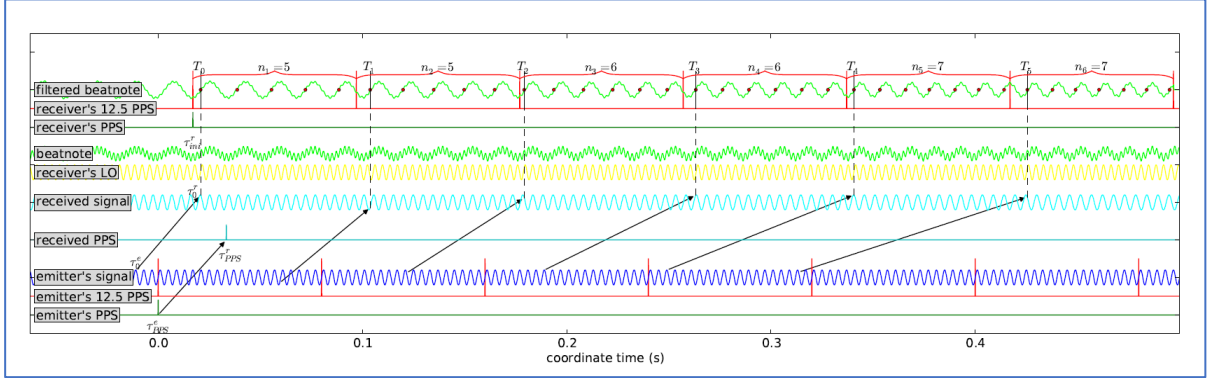
Figure 11. Schematic representation of the measurements provided by the modems.
Credit: Delva P., Laurent P., Le Poncin-Lafitte C., Meynadier F., Wolf P., 2012.

From these TT observables, it is possible to obtain the so-called ST observables (thus, the previously discussed PToF) which can be generically expressed as:

$$\Delta \tau^r(\tau^r) = \tau^e - \tau^r$$

(2 . 3)

where τ^e is the local time of the emitter and τ^r is the local time of the receiver of the signal. By implying the obtained TT observables, it is possible to determine the expression of the ST observable corresponding to the m sequence:

$$\Delta \tau_m^r(T_m) = \Delta \tau_{m-1}^r(T_{m-1}) + \left(\frac{\omega_{L.O.}}{\omega_e} - 1\right)(T_m - T_{m-1}) \pm \frac{2\pi n_m}{\omega_e}$$

(2 . 4)

This recursive formula[14] allows to find all ST observables (or PToF) from TT observables, if the first term $\Delta \tau_0^r(T_0)$ is known (Delva P., Laurent P., Le Poncin-Lafitte C., Meynadier F., Wolf P., 2012).

---

[14] The "$\pm$" is due to the fact that signs are different for code and carrier: "+" for the carrier and "−" for the code.

At this point, starting from the founded observables, the primary goal is to precisely determine a set of physical variables which represent the scientific products of the mission:

- the Total Electron Content, in order to determine and compensate for the ionospheric delay.

- the coordinated instantaneous distance between the two stations.

- the tropospheric delay, denoted as Δ^{tropo}.

- the desynchronisation of the clocks at a desired coordinate time t.

As a matter of fact, since the main contributions to the PToF are the desynchronisation between the ground and space clocks and the propagation delay, one is able to determine this desynchronisation. Therefore, this requires a model of the space-time geometry, a convention for defining the simultaneity of events, as well as a model for the propagation of the signal which takes into account atmospheric and instrumental delays (provided by on-ground calibration). Consequently, the positions of the ground and space stations have to be known to some level of accuracy in order to calculate the time-of-fight. The analysis will now touch the theoretical description of two distinct cases in relation to code observables: a one-way link and a two-way link.

a. One-way link

A one-way link between a ground g and a space clock s can be represented as in Figure 12. At coordinate time t_1, clock g displays time τ_1 and modem Mg produces a code C^1. This code modulates a sinusoidal signal of frequency f and sent at coordinate time t_2 by antenna g. The delay between the code production and its transmission by antenna g is $\Delta^g = [T_{12}]^g$, expressed in the local frame of clock g. Antenna s receives signal C^1 at coordinate time t_3 and transmits it to modem Ms and clock s which receives it at coordinate time t_4, with a delay $\Delta^s = [T_{34}]^s$ expressed in the local frame of clock s^{15}. The codes produced by the ground and the space clocks are the same, meaning that for the same proper time displayed by the clocks the same piece of code is produced. This is an unambiguous way to synchronise the signal to the proper

---

[15] More in general, $[T_{12}]^A$ is the transformation of coordinate time interval T_{12} in proper time of clock A and $[\Delta\tau^A]^t$ is the transformation of proper time interval of clock A in coordinate time t.

time of the clocks. We implicitly define the coordinate time t_5 when clock s displayed the same code C^1 as encoded in the received signal.

$$\tau_1 = \tau^g(t_1) = \tau^s(t_5)$$

(2.5)

Therefore, the ST observable (PToF) given by the receiver s is defined as:

$$\Delta\tau^s\big(\tau^s(t_4)\big) = \tau^s(t_5) - \tau^s(t_4)$$

(2.6)

From this, the desynchronisation between clock g and s can be written as:

$$\tau^s(t_4) - \tau^g(t_4) = -\Delta\tau^s\big(\tau^s(t_4)\big) - [T_{23} + [\Delta^g + \Delta^s]^t]^g$$

(2.7)

(a) Sequence of events
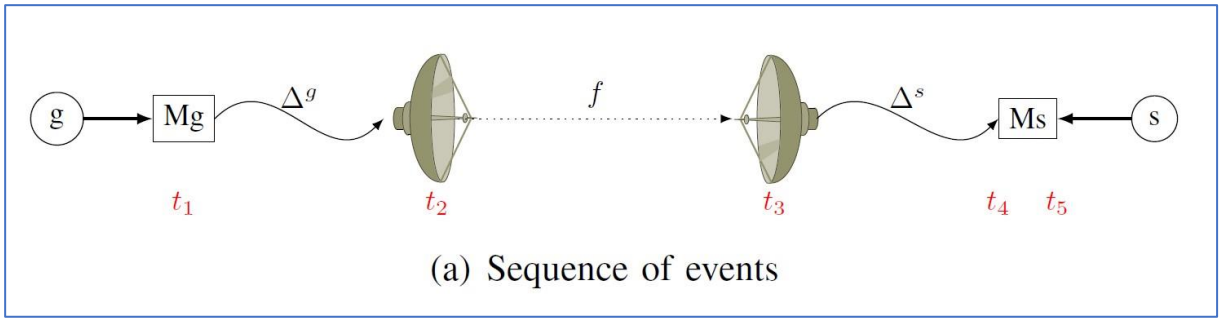
Figure 12. Scheme of the one-way link.
Credit: Delva P., Laurent P., Le Poncin-Lafitte C., Meynadier F., Wolf P., 2012.

b. Two-way link

By following the same reasoning as before, in a two-way link between a ground g and a space clock s, as depicted in Figure 13, the uplink from ground to space has a frequency f_1 and is characterised by the relation

$$\tau^g(t_1^0) = \tau^s(t_7^0)$$

(2.8)

while the downlink from space to ground at a frequency f_2 is characterised by the relation

$$\tau^s(t_3^0) = \tau^g(t_8^0)$$

(2.9)

As previously written, in the case of ACES/PHARAO a Λ configuration is implied in which $t_2 = t_3$, so that code C^2 of link f_2 is sent at antenna s when code C^1 of link f_1 is received at

this antenna. Finally, it can be shown that in this configuration the desynchronisation between the ground and the space clocks at coordinate time t_2 can be expressed as:

$$\tau^s(t_2) - \tau^g(t_2) = \frac{1}{2}\left(\Delta\tau_{mo}^g(t_4^0) - \Delta\tau_{mo}^s(t_2^0) + [T_{34} - T_{12}]^g\right)$$

<div align="right">(2. 10)</div>

where

$$\Delta\tau_{mo}^g(t_4^0) = \Delta\tau^g\left(\tau^g(t_4^0)\right) + \Delta_2^g + \Delta_2^s$$

<div align="right">(2. 11)</div>

$$\Delta\tau_{mo}^s(t_2^0) = \Delta\tau^s\left(\tau^s(t_2^0)\right) + \Delta_1^g + \Delta_1^s$$

<div align="right">(2. 12)</div>
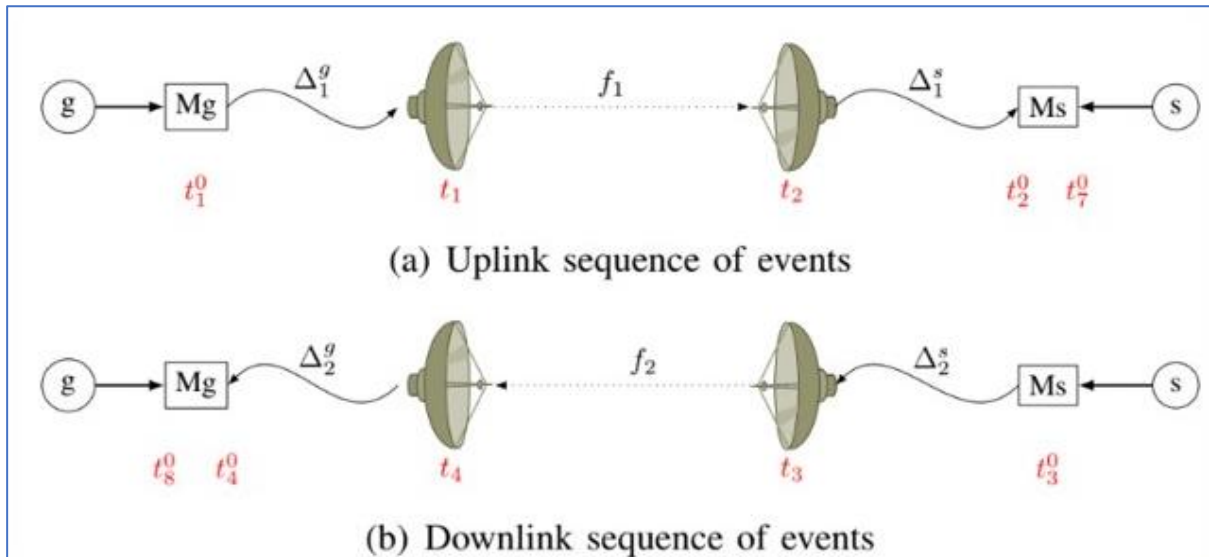
Figure 13. Scheme of the two-way link.
Credit: Delva P., Laurent P., Le Poncin-Lafitte C., Meynadier F., Wolf P., 2012.

The two links composing the downlink are affected by an ionospheric delay which depends on their respective frequencies f_2 and f_3, whereas the tropospheric delay does not depend on the link frequency. Dispersive troposphere effects are neglected in this case, although they can be taken into account using a global model (Baron P., Hobiger T., Piester D., 2013). Therefore, it is possible to define the overall propagation delays for the three links, including the atmospheric components, as:

$$T_{12} = \frac{R_{21}}{c} + \Delta_{12}^{iono}(f_1) + \Delta_{12}^{tropo} + \Delta_{21}^{Shapiro}$$

$$(2.13)$$

$$T_{34} = \frac{R_{34}}{c} + \Delta_{34}^{iono}(f_2) + \Delta_{34}^{tropo} + \Delta_{34}^{Shapiro}$$

$$(2.14)$$

$$T_{56} = \frac{R_{56}}{c} + \Delta_{56}^{iono}(f_3) + \Delta_{56}^{tropo} + \Delta_{56}^{Shapiro}$$

$$(2.15)$$

where $R_{ij} = |\vec{x_g}(t_j) - \vec{x_s}(t_i)|$ is the range, $\vec{x_s}$ and $\vec{x_g}$ are respectively the position vectors of space and ground antennas, $r_s = |\vec{x_s}|$, $r_g = |\vec{x_g}|$ and

$$\Delta_{ij}^{Shapiro} = \frac{2GM}{c^3} \ln\left(\frac{r_s(t_i) + r_g(t_j) + R_{ij}}{r_s(t_i) + r_g(t_j) - R_{ij}}\right) + \mathcal{O}(c^{-4})$$

$$(2.16)$$

Ionospheric and tropospheric delays are around or below 100 ns, whereas Shapiro delay is below 10 ps (Duchayne L., 2008).

With the aim of deducing the ionospheric delay, we can combine the two ground observables in order to be free of tropospheric delays in the following way:

$$\Delta\tau^g\left(\tau^g(t_6^0)\right) - \Delta\tau^g\left(\tau^g(t_4^0)\right) = [T_{34} - T_{56}]^s + [T_{46}^0]^s - [T_{46}^0]^g + \Delta_2^s - \Delta_3^s + \left[[\Delta_2^g - \Delta_3^g]^t\right]^s$$

$$(2.17)$$

By imposing $T_{46}^0 = 0$, with a resulting uncertainty of $\delta T_{46}^0 < 0.9\ ms$ and through some approximations (Duchayne L., 2008 and Delva P., Laurent P., Le Poncin-Lafitte C., Meynadier F., Wolf P., 2012), we get the expression:

$$\Delta\tau_{mo}^g(t_6^0) - \Delta\tau_{mo}^g(t_4^0) = T_{34} - T_{56}$$

$$(2.18)$$

Finally, we obtain:

$$\Delta_{56}^{iono}(f_3) - \Delta_{34}^{iono}(f_2) = \Delta\tau_{mo}^g(t_4^0) - \Delta\tau_{mo}^g(t_6^0) + \frac{R_{34} - R_{56}}{c}$$

$$(2.19)$$

Now we can calculate the Slant Total Electron Content (STEC), denoted as S. The ionospheric delay affects oppositely code (co) and carrier (ca) and can be approximated as follows through a Chapman layer STEC model:

$$\Delta_{co}^{iono}(f) = \frac{40.308}{cf^2}S + \frac{7527}{f^3}\int N_e(\overrightarrow{B}\cdot\overrightarrow{k})\,dL$$

$$\Delta_{ca}^{iono}(f) = -\frac{40.308}{cf^2}S - \frac{7527}{2f^3}\int N_e(\overrightarrow{B}\cdot\overrightarrow{k})\,dL$$

where N_e is the local electron density along the path, STEC $S = \int N_e dL$, $\overrightarrow{B}$ is the Earth's magnetic field and $\overrightarrow{k}$ is the unit vector along the signal propagation direction. Considering the three observables $\Delta\tau^s(\tau^s(t_2^0))$, $\Delta\tau^g(\tau^g(t_4^0))$, $\Delta\tau^g(\tau^g(t_6^0))$, we suppose that $\vec{B}$ and $\vec{k}$ do not change along the signals Line of Sight and $|\vec{B}| \cong B_0$, we can write that:

$$\Delta_{co}^{iono}(f) = \frac{40.308}{cf^2}S\left(1 + \frac{7527c}{40.308f}B_0\cos\theta_0\right)$$

$$\Delta_{ca}^{iono}(f) = -\frac{40.308}{cf^2}S\left(1 + \frac{7527c}{80.616f}B_0\cos\theta_0\right)$$

where θ_0 is the angle between $\vec{B}$ and the propagation direction of the signals f_2 and f_3. Finally, we obtain:

$$\left[\Delta_{56}^{iono}(f_3) - \Delta_{34}^{iono}(f_2)\right]_{co} = \frac{40.308}{c}\left(\frac{1}{f_3^2} - \frac{1}{f_2^2}\right)S \times \left[1 + \frac{7527c}{40.308}\frac{f_2^3 - f_3^3}{f_2 f_3(f_2^2 - f_3^2)}B_0\cos\theta_0\right]$$

$$\left[\Delta_{56}^{iono}(f_3) - \Delta_{34}^{iono}(f_2)\right]_{ca} = -\frac{40.308}{c}\left(\frac{1}{f_3^2} - \frac{1}{f_2^2}\right)S \times \left[1 + \frac{7527c}{80.616}\frac{f_2^3 - f_3^3}{f_2 f_3(f_2^2 - f_3^2)}B_0\cos\theta_0\right]$$

By equating these equations with the one found before, we can determine the expression of the STEC S and correct the ionospheric delay.

On the other hand, when dealing with tropospheric delay, we combine the ground and space observables of links f_1 and f_2 in the following way:

$$\Delta\tau^s(\tau^s(t_2^0)) + \Delta\tau^g(\tau^g(t_4^0)) + \Delta_1^g + \Delta_2^g + [[\Delta_1^s + \Delta_2^s]^t]^g = [T_{23}^0]^s - [T_{23}^0]^g - [T_{12} + T_{34}]^g$$

It can be shown that $[T_{23}^0]^s - [T_{23}^0]^g \cong 0$ if T_{23}^0 is known with an accuracy of $\delta T_{23}^0 < 0.9\ ms$. Thanks to a series of approximations, it is possible to derive the following expressions:

$$T_{12} + T_{34} = -\left(1 + \frac{GM}{r_g(t_2)c^2}\right)\left(\Delta\tau_{mo}^s(t_2^0) + \Delta\tau_{mo}^g(t_4^0)\right)$$

(2.27)

$$\frac{R_{21} + R_{34}}{c} = -\left(1 + \frac{GM}{r_g(t_2)c^2}\right)\left(\Delta\tau_{mo}^s(t_2^0) + \Delta\tau_{mo}^g(t_4^0)\right)$$
$$- \left(\Delta_{12}^{iono}(f_1) + \Delta_{34}^{iono}(f_2) + \Delta_{12}^{tropo} + \Delta_{34}^{tropo}\right)$$

(2.28)

This equation shows that range can be computed thanks to a model of tropospheric delay, while tropospheric delay can be computed through an estimation of range. In other words, the two quantities are degenerate (Duchayne L., 2008 and Delva P., Laurent P., Le Poncin-Lafitte C., Meynadier F., Wolf P., 2012).

2.2. From ACES mission to a possible new one-way configuration

In the first chapter, we have tackled the deep interest of the scientific community in searching for a one-way architecture to allow the communication between the ground and a spacecraft in a more efficient way with the ultimate goal of enabling spacecraft to autonomously navigate in space. In this sense, the model developed for the ACES mission has embodied a starting point for the study conducted throughout this thesis in order to imagine a possible novel one-way uplink scenario. In case we aim at configuring the links of the ACES mission in a one-way uplink fashion, one of the problems involves the compensation of the atmospheric delays. As previously explained, in the Λ configuration both the ionospheric and the tropospheric delays expressions involve the combination of the ground and space observables. However, in a one-way uplink configuration we do not have a ground observable at our disposal anymore but only a space observable and, apparently, we cannot determine the expression for the STEC and, thus, for the ionospheric delay. Finally, we cannot determine an expression for the tropospheric delay either. To avoid this problem, we can think about a possible modification to the single-frequency one-way uplink of ACES. Since the S-band third frequency is added to determine the ionospheric delay and since the uplink frequency f_1 is in the same band as the ACES downlink frequency f_2 (Ku-band), we can think of configuring a dual-frequency one-way uplink, using:

$$f_1 \cong 13.5\ GHz$$

$$f_2 \cong 2.2\ GHz.$$
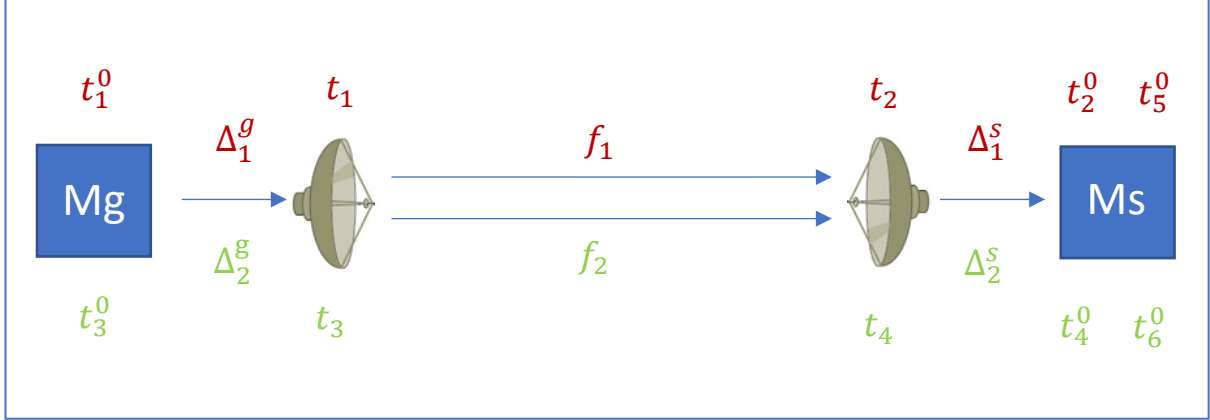
Figure 14. A possible scheme of the dual frequency one-way uplink. The two links are depicted in red and green.

In other words, we are transposing the two-frequency concept from the downlink to the uplink and we can assume that the previous equations concerning the ionospheric and tropospheric delay are still valid also in this configuration. The difference lies in the fact that, in this case, the computation of both the observables and the scientific products must be run on-board. The modem configuration must be changed as well because we would have four ST space observables, one for the code and one for the carrier for each of the two uplink frequencies f_1 and f_2. These ST observables are of the type expressed as:

$$\Delta\tau^s\big(\tau^s(t_2^0)\big) = \tau^s(t_5^0) - \tau^s(t_2^0)$$

$$(2.29)$$

$$\Delta\tau^s\big(\tau^s(t_4^0)\big) = \tau^s(t_6^0) - \tau^s(t_4^0)$$

$$(2.30)$$

To simplify the subsequent simulation of this scenario, we imagine computing these PToF through a correlation between the signal received onboard and a replica of the same signal locally generated by the spacecraft. As a matter of fact, at the moment of the correlation to be performed, the signal received will be delayed by a certain amount which includes a certain propagation delay T_{ij}, the delays related to the on-ground and onboard hardware and, finally, the discrepancy between the proper time of the spacecraft clock and the proper time of the ground clock. This last component represents the desynchronisation between the two clocks at

a certain coordinate time t. For example, considering the link f_1 (the same applies to the link f_2), the expression of the PToF computed at t_2^0, the reception time of the signal, is:

$$\Delta\tau^s\left(\tau^s(t_2^0)\right) = -\left(\tau^s(t_2^0) - \tau^g(t_2^0)\right) - \left[T_{12} + \left[\Delta_1^g + \Delta_1^s\right]^t\right]^g$$

$$(2.31)$$

where $\left(\tau^s(t_2^0) - \tau^g(t_2^0)\right)$ represents, indeed, the desynchronisation. From this PToF, it is straightforward to state that the desynchronisation is provided by the following expression:

$$\left(\tau^s(t_2^0) - \tau^g(t_2^0)\right) = -\Delta\tau^s\left(\tau^s(t_2^0)\right) - \left[T_{12} + \left[\Delta_1^g + \Delta_1^s\right]^t\right]^g$$

$$(2.32)$$

Once the desynchronisation is determined, it is possible to "steer" the time reported by the spacecraft clock to the correct value, which is the one of the ground station at t_1^0, so that:

$$\tau^s(t_5^0) = \tau^g(t_1^0)$$

$$(2.33)$$

Obviously, if we want to determine the desynchronisation, it is necessary to derive T_{ij} which is expressed as:

$$T_{ij} = \frac{R_{ij}}{c} + \Delta_{ij}^{iono}(f) + \Delta_{ij}^{tropo}$$

$$(2.34)$$

where the Shapiro effect is neglected since it provides a very low contribution to the overall delay. As in ACES mission, the positions of the ground station and the spacecraft have to be known to some level of accuracy in order to calculate the time-of-fight onboard. First of all, the geometric range R_{ij} can be determined as explained before, whereas the ionospheric delay can be obtained thanks to the exploitation of the two observables available at the space station. Indeed, we look for an expression of the STEC, so that a correction of the ionospheric delay itself is made possible:

$$T_{12} - T_{34} = \Delta\tau^s\left(\tau^s(t_4^0)\right) - \Delta\tau^s\left(\tau^s(t_2^0)\right) + \Delta_2^g - \Delta_1^g + \Delta_2^s - \Delta_1^s + \int_{t_1}^{t_2} E_g(t)dt - \int_{t_3}^{t_4} E_g(t)dt$$

$$(2.35)$$

where $\int_{t_i}^{t_j} E_g(t)dt = \int_{t_i}^{t_j} \left(\frac{U(t,\vec{x_g})}{c} + \frac{v_g^2(t)}{2c^2}\right)dt$ represents the correction for the proper/coordinate time transformation. Therefore, if we consider the tropospheric delays for the two uplink signals as equal, we can write that:

$$\Delta_{34}^{iono}(f_2) - \Delta_{12}^{iono}(f_1)$$

$$= \Delta\tau^s\big(\tau^s(t_2^0)\big) - \Delta\tau^s\big(\tau^s(t_4^0)\big) + \Delta_1^g - \Delta_2^g + \Delta_1^s - \Delta_2^s$$

$$- \int_{t_1}^{t_2} E_g(t)dt + \int_{t_3}^{t_4} E_g(t)dt + \frac{R_{12} - R_{34}}{c}$$

$$(2.36)$$

Assuming that the previously used Chapman layer STEC model is still valid to approximate the ionospheric delay, we can express:

$$S = \pm\left(\frac{c}{40.308 * F(f_1, f_2, c, B_0, \theta_0)} * \frac{f_2^2 * f_1^2}{f_1^2 - f_2^2}\right)$$

$$\times \left[\left(\Delta\tau^s\big(\tau^s(t_2^0)\big) - \Delta\tau^s\big(\tau^s(t_4^0)\big)\right) + (\Delta_1^g - \Delta_2^g) + (\Delta_1^s - \Delta_2^s)\right.$$

$$\left. - \int_{t_1}^{t_2} E_g(t)dt + \int_{t_3}^{t_4} E_g(t)dt + \frac{R_{12} - R_{34}}{c}\right]$$

$$(2.37)$$

where

$$F(f_1, f_2, c, B_0, \theta_0) = \left[1 + \frac{7527 * c}{40.308 * 2} * \frac{f_1^3 - f_2^3}{f_1 * f_2 * (f_1^2 - f_2^2)} * B_0 * \cos\theta_0\right]$$

$$(2.38)$$

Since the leading term is represented by the difference between the two space observables, all other terms, which again represent differences, can be neglected and we still obtain an acceptable expression for S (Angonin M.C., Delva P., Guerlin C., Lilley M., Savalle E. et al., 2021):

$$S = \pm\left(\frac{c}{40.308 * F(f_1, f_2, c, B_0, \theta_0)} * \frac{f_2^2 * f_1^2}{f_1^2 - f_2^2}\right) \times \left[\Delta\tau^s\big(\tau^s(t_2^0)\big) - \Delta\tau^s\big(\tau^s(t_4^0)\big)\right]$$

$$(2.39)$$

Concerning the tropospheric delay, since now we have only two space observables and no ground observables, the only way to find an expression for this delay is to express it through a model. In particular, we can resort to a Saastamoinen model (Saastamoinen J., 1973), in the form:

$$\Delta^{tropo} = \frac{2.277 \times 10^{-3}}{c \cos z} \left[p + \left(0.05 + \frac{1255}{T} \right) e - (\tan z)^2 \right]$$

$$(2.40)$$

where p is the atmospheric pressure, T is the atmospheric temperature, e is the water vapour partial pressure and z is the angle between the line-of-sight and zenith, computed from the positions of the spacecraft and the ground station in the International Celestial Reference Frame (ICRF).

Finally, concerning the instrumental internal delays, they are needed for the determination of the desynchronisation between the ground clock and the space clock and, also, for an even more accurate estimation of the STEC S and, thus, of the ionospheric delays. We can assume that the ground delays are known and can be calibrated by sending them to the spacecraft or by phase advancing the signal before its transmission to space in order to pre-compensate these delays.

The next step to concretise such a one-way uplink framework is to verify the feasibility of a time transfer link between the ground station, equipped with an ultra-precise and stable clock and the spacecraft, equipped, on the contrary, with a clock characterised by a not so high temporal and frequency stability. In this way, it will be possible to significantly reducing the costs and complexity of the onboard payload, unlike other projects in which the presence of an extremely precise clock on-board the spacecraft is required. In particular, we can assume to open clock synchronisation windows, separated from each other by a certain time interval dt. The window begins with generation of the signal at the ground station and it is subsequently sent to the clock on-board the spacecraft. Once the two clocks show the same time reference, they are synchronised and, therefore, it is possible to take advantage of this synchronisation to be able to carry out the necessary radiometric measurements. Consequently, although the onboard clock might show an even accentuated temporal deviation with respect to the ground reference between one synchronisation window and the next (in other words, the onboard clock undergoes a temporal drift during this interval), it will be possible for ground control to not be concerned about it until the new synchronisation window, when new measurements will be taken. All of this would be particularly useful especially within those missions in deep space which involve long periods of cruise, during which the spacecraft can be left to continue along its trajectory while its clock experiences the time shift, synchronising it only on occasion of those "time critical" operations mentioned above but with all the aforementioned advantages of one-way uplink communication.

2.3. The simulator

As previously anticipated, a simulator has been developed in MATLAB programming language in order to preliminarily test the above-mentioned architecture, by using a simplified one-way uplink scheme and following the ACES model illustrated in the previous section. We investigate the feasibility of creating a connection for time transfer between an ultra-precise terrestrial clock and a spacecraft clock, which has comparatively lower temporal and frequency stability. Our method involves establishing clock synchronisation windows separated by a specific time interval dt, finally computing the error derived from this synchronisation process.

2.3.1. General structure

The script is a simplified simulation of a possible one-way uplink synchronisation scenario between a ground station clock and a clock mounted on-board a spacecraft to assess a preliminary accuracy measure of the synchronisation operation itself. At least for the time being, the spacecraft is assumed to travel with a constant speed **vs** in a straight direction, having an initial distance from the ground station on the Earth's surface specified in the parameter **init_distance**. Moreover, the ground station clock and the spacecraft clock are assumed to be initially synchronised at a generic time $t = 0$. The spacecraft clock is assumed to be a Temperature-Compensated Crystal Oscillator (TCXO[16]), a clock recently used for small-medium spacecrafts as a trade-off between cost, weight and stability, whose specifics are reported in the Appendix. The time deviation of the TCXO is represented in Figure 15. The Allan deviation (ADEV) is the square root $\sigma_y(\tau)$ of the so-called Allan variance, the most common time domain measure of frequency stability. It is defined as (Riley W., 2008):

$$\sigma_y^2(\tau) = \frac{1}{2(M-1)} \sum_{i=1}^{M-1} [y_{i+1} - y_i]^2$$

(2. 41)

where y_i is the i-th of M fractional frequency values averaged over the measurement (sampling) interval τ.

---

[16] A TCXO is a temperature-compensated crystal oscillator which is used whenever a certain stability within a variant temperature environment is required, i.e., when the frequency deviation of the oscillator must be minimal over its entire operating temperature range.

On the other hand, the time Allan variance, TVAR, with square root TDEV, is a measure of time stability based on the Allan variance and it is defined as (Riley W., 2008):

$$\sigma_x^2(\tau) = \left(\frac{\tau^2}{3}\right) Mod \, \sigma_y^2(\tau)$$

(2. 42)

where $Mod \, \sigma_y^2(\tau) = \frac{1}{2m^4(M-3m+2)} \sum_{j=1}^{M-3m+2}\{\sum_{i=j}^{j+m-1}(\sum_{k=i}^{i+m-1}[y_{k+m} - y_k])\}^2$. In particular, a time deviation of 10^{-10} was chosen, represented by the parameter **time_dev_coeff**, resulting in a time drift of $10^{-10} * \sqrt{\tau}$, where τ is the integration time. At some point, a synchronisation window starts, during which a signal is sent from the ground to the spacecraft reporting the reference time of the ground clock itself. Once the signal is received, it is cross-correlated with a local replica generated on-board to determine the overall PToF observable, simply denoted as **delay_obs**, comprising the propagation delay, the hardware delays and the desynchronisation between the two clocks. In particular, the internal hardware delays must be determined as well as the distance between the ground station clock and the spacecraft clock in order to derive the propagation delay. In this sense, considering the dual frequency model examined before, the atmospheric delays (ionospheric delay and tropospheric delay) are assumed to be compensated with an acceptable level of accuracy for the sake of simplicity in the simulation. Once the hardware and the propagation delays have been computed with some levels of white noise (representing the uncertainties in the estimation), they are subtracted from the computed PToF observable, so that the desynchronisation can be deduced. At this point, it is possible to bring the spacecraft clock to the correct value and synchronise it. In the end, the difference between the transmitted initial ground clock time and the new synchronised spacecraft clock time is computed with the purpose of determining the synchronisation error, both in terms of seconds and meters (to also account for the error on the range measurement). Once the synchronisation error has been determined, the spacecraft clock will drift in time once again until another synchronisation window will be opened after a time interval specified by the parameter **dt**.
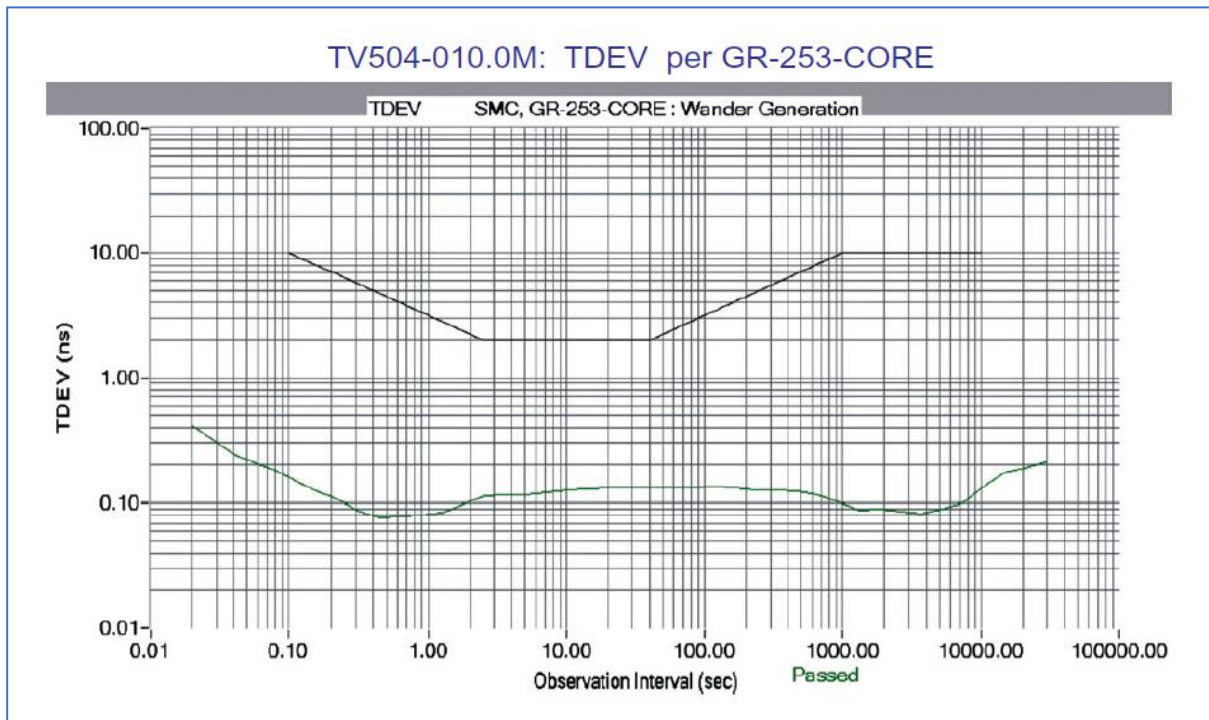
Figure 15. Time deviation (TDEV) of the considered TCXO.
Credit: Connor-Winfield.

The simulator is structured in such a way that we can select the number of successive synchronisation windows to simulate through the parameter **n_synch_win**. The different windows are separated by an interval **dt**, expressed in seconds. Many simulations are performed for the different synchronisation windows and this number can be set through the parameter **n_sim**. By doing so, the final values of the synchronisation error for each synchronisation window are computed through a Root Mean Square of a consistent set of results. In addition, distinct values of the **dt** interval which separates two consecutive synchronisation windows have been tested, with the aim of observing the trend of the synchronisation error in relation to them. With the purpose of evaluating the overall performance, a series of graphs have been plotted to appreciate the evolution of the aforementioned values as a function of time. These graphs will be shown and discussed in the next chapter.

2.3.2. Initial setting and computations

At the beginning of the simulation of the first synchronisation window, the **ground_time** is simply set equal to the time passed since the spacecraft leaves the Earth, which is equal to the actual distance of the spacecraft divided by the speed of the spacecraft itself. As a consequence, the propagation time, denoted as **propagation_time_one_way**, is set equal to the distance divided by the speed of light **c**. On the other hand, the spacecraft time, denoted as **space_time**, drifts from the reference ground time as a function of its time deviation, following the relation $10^{-10} * \sqrt{\tau}$.

$$ground\ time = \frac{distance_{init}}{v_s}$$

$$(2.\ 43)$$

$$space\ time = \frac{distance_{init}}{v_s} + \left(time\ dev * \sqrt{\frac{distance_{init}}{v_s}} \right)$$

$$(2.\ 44)$$

$$propagation\ time\ one\ way = \frac{distance_{init}}{c}$$

$$(2.\ 45)$$

Afterwards, random hardware delays Δ^g and Δ^s are generated, uniformly distributed in a specified interval $[a, b]$, using the MATLAB function **rand**. At this point, the distance and, therefore, the propagation delay must be "corrected", since the spacecraft keeps moving as the signal propagates through space.

$$distance = distance + v_s * \left(\frac{distance}{c} + \Delta^g \right)$$

$$(2.\ 46)$$

$$propagation\ time = \frac{distance}{c}$$

$$(2.\ 47)$$

In this way, the actual ground clock and spacecraft clock times can be derived, together with the desynchronisation between them (computed at the spacecraft once the signal is received), denoted as **desynchronisation_true**.

$$ground\ time = ground\ time\ +\ propagation\ time\ +\ \Delta^g + \Delta^s$$

<div align="right">(2. 48)</div>

$$space\ time\ =\ space\ time + propagation\ time + \Delta^g + \Delta^s \\ +\ time\ dev * \sqrt{propagation\ time + \Delta^g + \Delta^s}$$

<div align="right">(2. 49)</div>

$$desynchronisation_{true} = space\ time - ground\ time$$

<div align="right">(2. 50)</div>

2.3.3. Cross-correlation between the received signal and the local replica

In order to compute the onboard PToF observable, a sinusoidal signal is generated in MATLAB with a certain sampling frequency **fs**. For computational reasons, the cosine function is generated at a low frequency of 1 kHz, in order not to slow down the simulations but being anyway sufficient to our purposes. Some AWGN noise is generated through the MATLAB function **randn** and it is added to the signal to reproduce the channel encountered during its propagation. Moreover, the sinusoid is delayed by a certain value denoted as **total_delay**, including all delays to which the signal is subjected in its travel from the ground station towards the spacecraft. In particular, the delay is introduced thanks to the MATLAB function **delayseq(data, delay, fs)** which delays or advances the signal in **data** by the number of samples specified in **delay** and taking into account the sampling frequency **fs**. Since **total_delay** is not, in general, an integer number, the function interpolates between samples. Afterwards, the correlation between the local replica and the received noisy and delayed signal is computed through the MATLAB function **xcorr(x,y)** which, indeed, returns the cross-correlation of two discrete-time sequences **x** and **y**. Specifically, cross-correlation measures the similarity between a vector **x** and shifted (lagged) copies of a vector **y** as a function of the lag[17]. The final PToF observable is derived by considering the lag, thus, the time delay, corresponding to the maximum correlation value.

---

[17] <https://it.mathworks.com/help/matlab/ref/xcorr.html>.

$$total\ delay\ =\ propagation\ time\ +\ desynchronisation_{true}\ +\ \Delta^g\ +\ \Delta^s$$

<div align="right">(2.51)</div>

$$signal = \cos{(2pi * f * t)}$$

<div align="right">(2.52)</div>

$$delayed\ signal\ =\ delayseq(signal, total\ delay, fs)$$

<div align="right">(2.53)</div>

$$signal_{received}\ =\ delayed\ signal\ +\ awgn\ channel\ noise$$

<div align="right">(2.54)</div>

$$correlation = xcorr(signal, signal_{received})$$

<div align="right">(2.55)</div>

Through different tests, it emerged that above a certain number of delay samples, 1000 in our case, the **xcorr** MATLAB function had some problems in computing the correlation between the original signal and the delayed one, providing an erroneous value of the observable. For this reason, a "manual" correction was required, so that for delays above 1000 samples the delay introduced on the sinusoid is halved to allow the **xcorr** to properly compute the correlation. Subsequently, the derived observable is doubled to obtain the correct value. Obviously, this approximation method inserts some error in the overall synchronisation process but it is acceptable, as can be observed in the graphs in the next chapter.

2.3.4. Determination of the desynchronisation

At this stage, the value of the desynchronisation between the ground and the spacecraft clocks is derived by subtracting the hardware and the propagation delays from the founded PToF observable, reproducing the equations of the theoretical model of ACES. With the aim of simulating the uncertainties in the estimation and calibration of the delays, some normal noise is generated through the function **randn** with the variances specified in the parameters **sigma_noise_delays** and **sigma_noise_distance**, respectively.

$$distance_{meas} = distance + normal\ noise\ distance$$

<div align="right">(2.56)</div>

$$propagation\ time_{meas} = \frac{distance_{meas}}{c}$$

<div align="right">(2. 57)</div>

$$\Delta_{meas}^{g} = \Delta^{g}\ +\ normal\ noise\ delays_1$$

<div align="right">(2. 58)</div>

$$\Delta_{meas}^{s} = \Delta^{s}\ +\ normal\ noise\ delays_2$$

<div align="right">(2. 59)</div>

$$desynchronisation_{meas}\ = -PToF - (propagation\ time_{meas}\ + \Delta_{meas}^{g} + \Delta_{meas}^{s})$$

<div align="right">(2. 60)</div>

Thanks to the desynchronisation, it is possible to set the spacecraft time to the correct value. Finally, the synchronisation error can be deduced by the absolute value of the difference between the initial ground time, the one transmitted by the ground station at the beginning of the synchronisation window, and the synchronised spacecraft time.

$$Synch\ error = abs(ground\ time_{init} - space\ time)$$

<div align="right">(2. 61)</div>

Chapter 3: Results

As described in the previous chapter, a series of graphs have been plotted to observe the evolution of the aforementioned synchronisation error values as a function of time. Moreover, it is possible to appreciate the trend of the average synchronisation error obtained for the set of synchronisation windows, as a function of an increasing dt.

In the subsequent Figures it is possible to see the evolution of the synchronisation error as a function of time for several lengths of the interval in between two consecutive synchronisation windows. The sampling frequency for the generation of the signal in MATLAB and for the computation of the correlation is set to $f_s = 10^6$, whereas the number of simulations is set to 1000. From the several tests conducted on the simulated scenario, it emerged that we must start to synchronise the spacecraft clock, which means to open the first synchronisation window, when the space vehicle is not so far from the Earth (from 200 kilometres up to 500 kilometres), so that the clock drift does not become immediately irrecoverable. Afterwards, we can assume to leave the spacecraft continue on its trajectory towards the destined target and we will reopen a new synchronisation process when needed, so that, once the spacecraft clock will be synchronised again, new radiometric observables will be measured. In the following graphs, the considered initial distance is the minimum tested one, set equal to 200 kilometres. Moreover, a significant number of synchronisation windows is examined, set equal to 50. It is important to highlight the fact that, as long as we increase the value of dt, we observe an increment of the synchronisation error. This is due to the fact that, by enhancing the interval between two consecutive windows, the spacecraft clock has the possibility to "drift more" during that period, travelling a longer distance, so that it is harder to recover the resulting desynchronisation with respect to the ground clock. As a matter of fact, this is evident in the transition from the graph corresponding to $dt = 60 \, s$ or $dt = 120 \, s$ to the graph corresponding to $dt = 200 \, s$, since the synchronisation error in seconds moves from an order of magnitude of 10^{-7} seconds to an order of magnitude of 10^{-6} seconds. As a consequence, also the error expressed in meters increases accordingly.

Figure 16. Synchronisation error expressed in seconds as a function of time, with $dt = 60\ s$ and $fs = 10^6$.

Figure 17. Synchronisation error expressed in seconds as a function of time, with $dt = 120\ s$ and $fs = 10^6$.

47

Figure 18. Synchronisation error expressed in seconds as a function of time, with $dt = 200\ s$ and $fs = 10^6$.
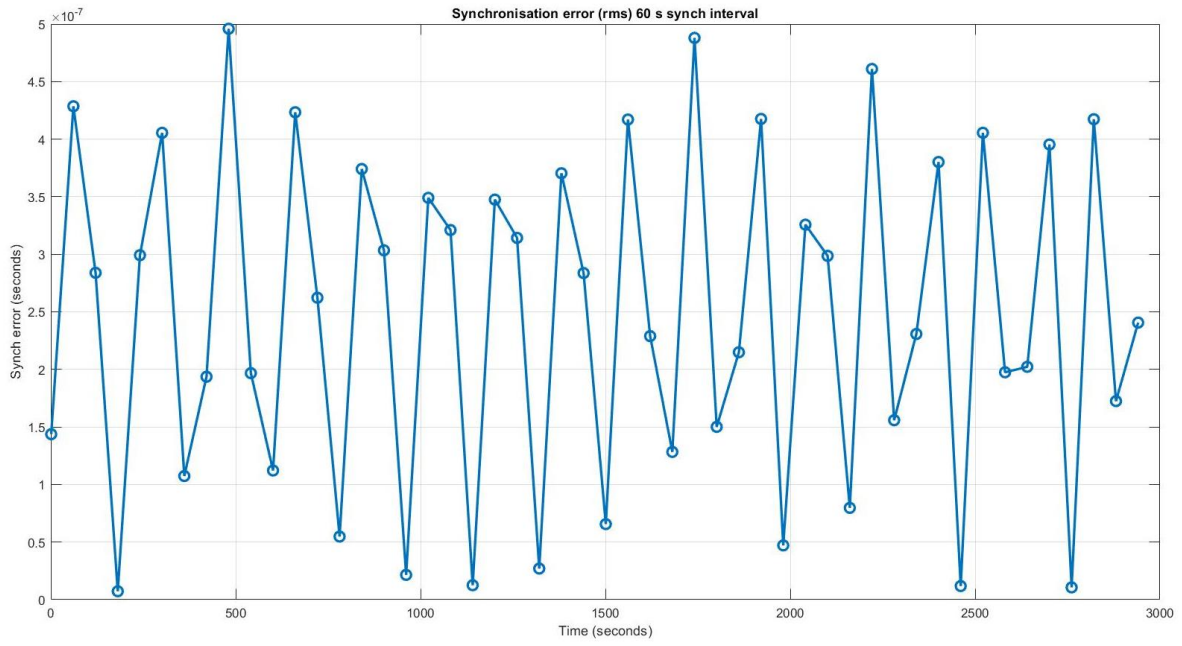

Figure 19. Synchronisation error expressed in meters as a function of time, with $dt = 60\ s$ and $fs = 10^6$.
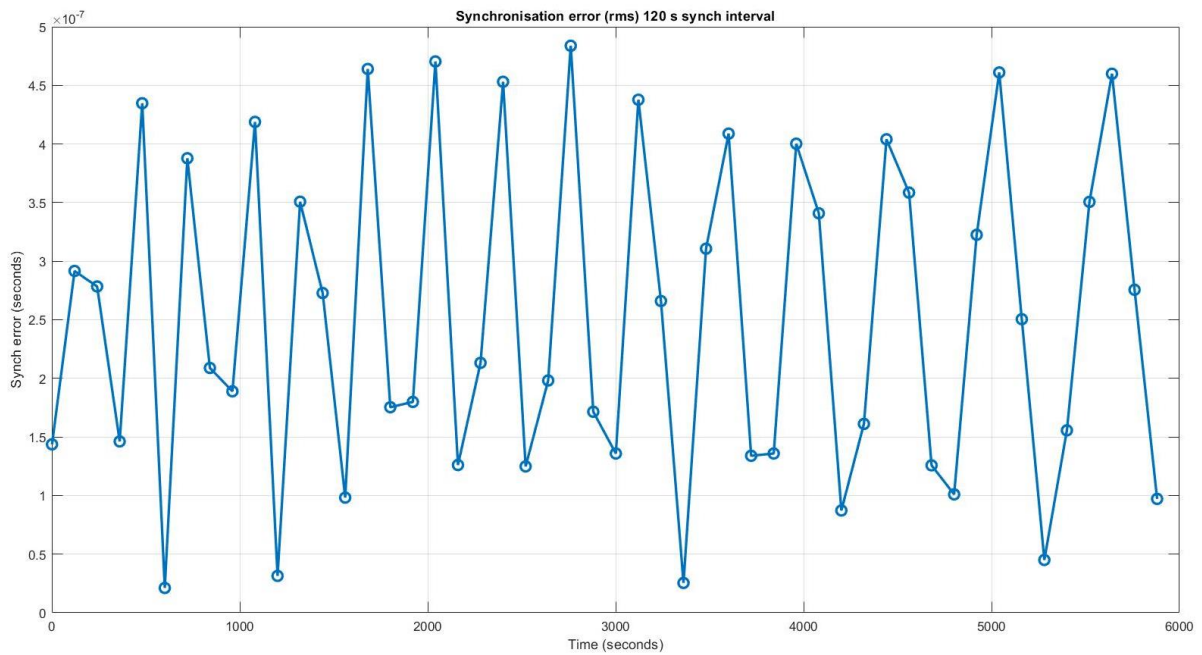
Figure 20. Synchronisation error expressed in meters as a function of time, with $dt = 120\ s$ and $fs = 10^6$.
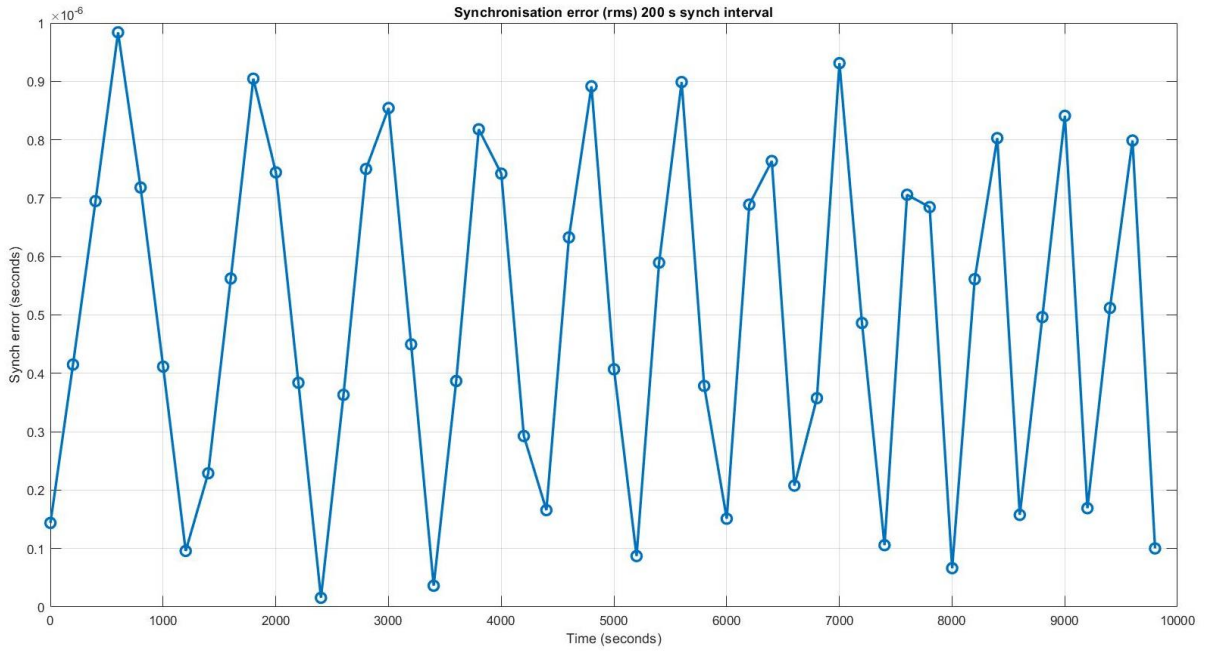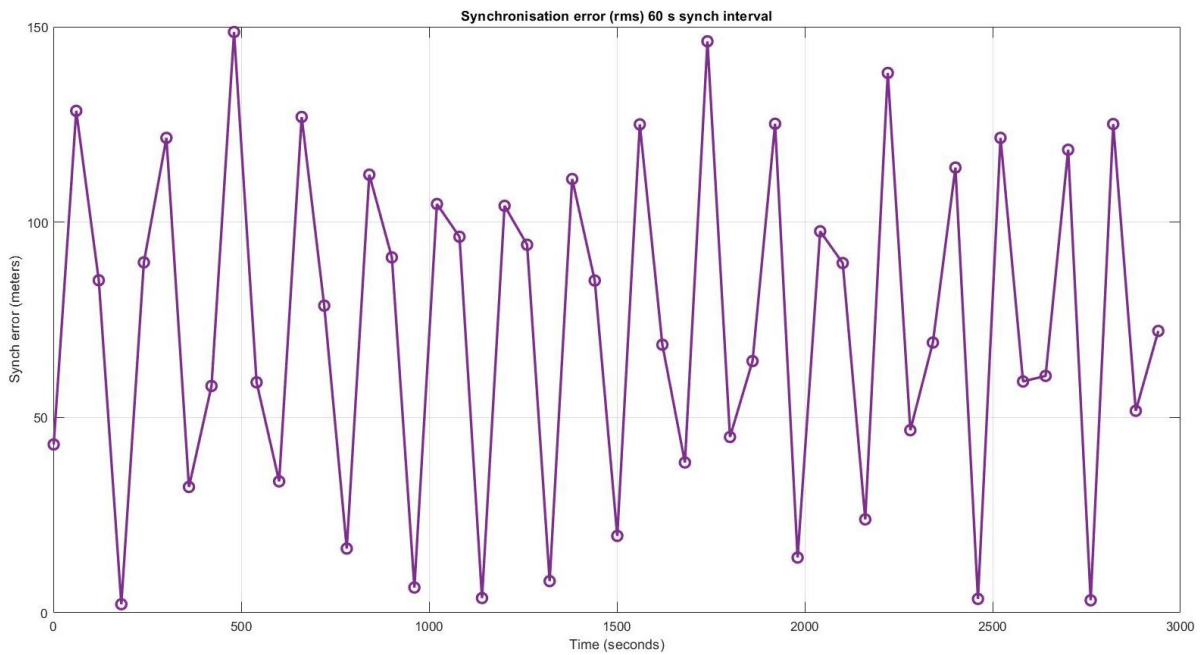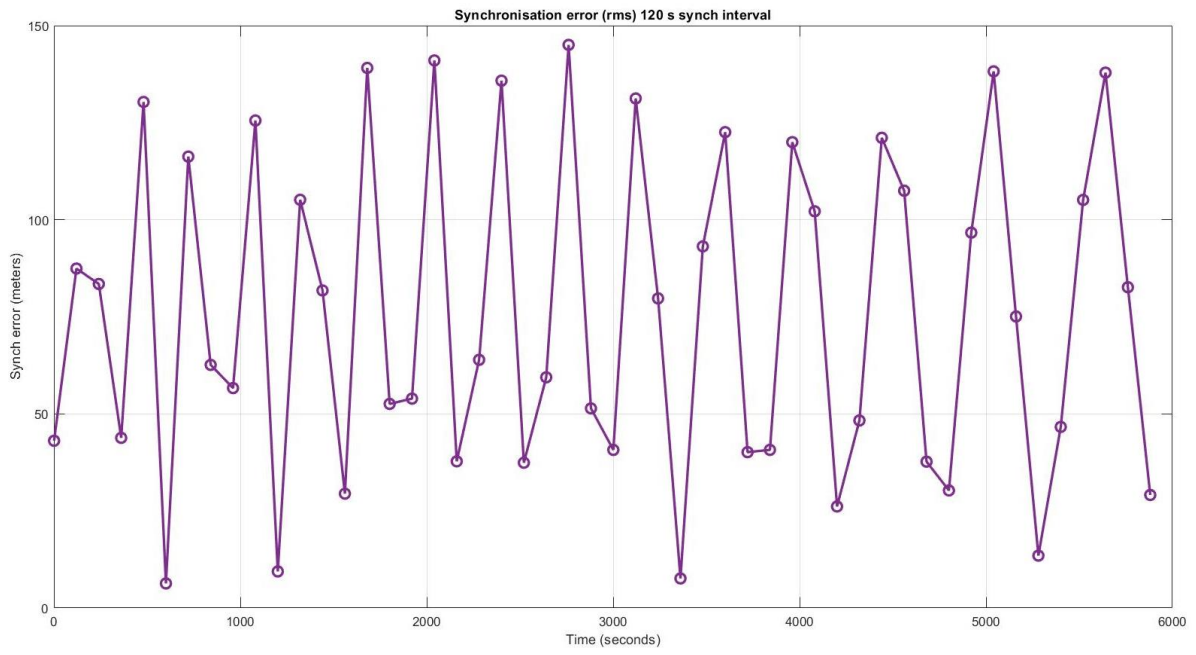

Figure 21. Synchronisation error expressed in meters as a function of time, with $dt = 200\ s$ and $fs = 10^6$.

In Figure 22 and Figure 23, we can see the Mean Synchronisation Error, both in terms of seconds and meters. In particular, the average is computed taking into account the RMS values which result from the entire set of simulations for each of the tested synchronisation windows. In fact, after the completion of all simulations, we get a matrix of dimensions (n° of simulations, n° of synchronisation windows). Later, we compute the RMS values over the columns of the matrix, obtaining a row vector of dimensions (1, n° of synchronisation windows). Finally, we compute the mean value of this vector in order to have a single star point on the graph for each of the tested length of the time interval dt. In these graphs, a sampling frequency $f_s = 10^6\ Hz$ is used for the generation of the discrete signal in MATLAB and in the computation of the correlation and 1000 simulations are implied for each of the synchronisation window. As shown by the graphs, it is possible to note an increase, yet small, of the Mean Synchronisation Error. The evident "jump" upwards is due to the aforementioned "manual" correction which is needed from 1000 delay samples on but it is still acceptable because all values remain in the same order of magnitude.
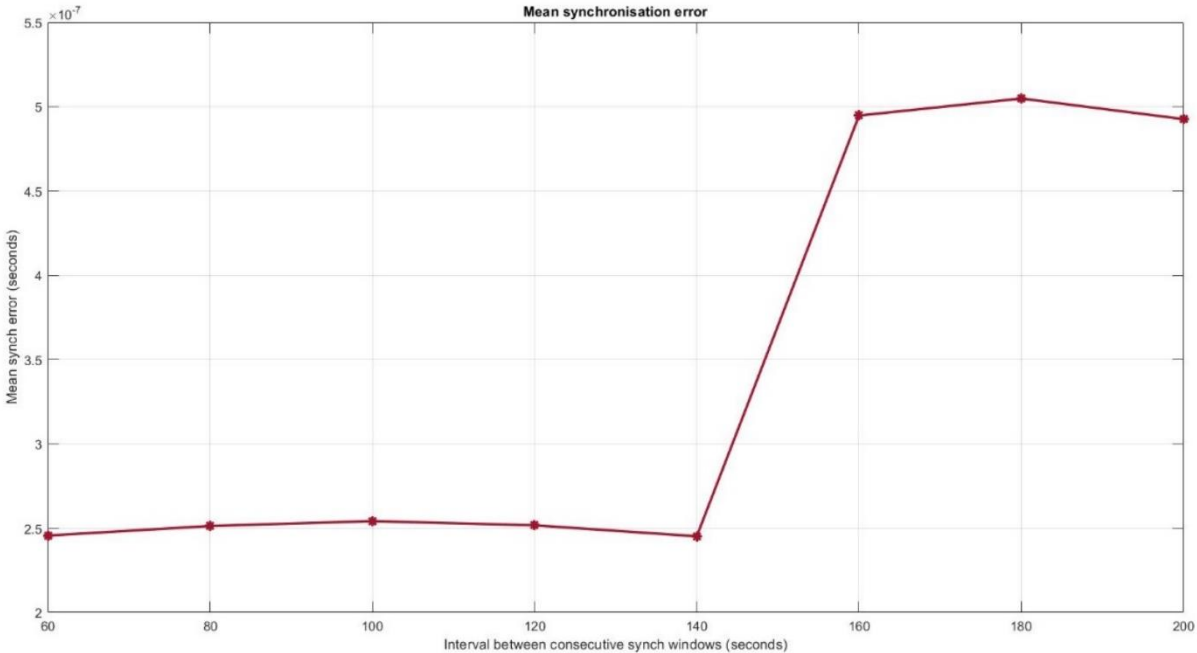
Figure 22. Mean synchronisation error expressed in seconds, with $fs = 10^6$.
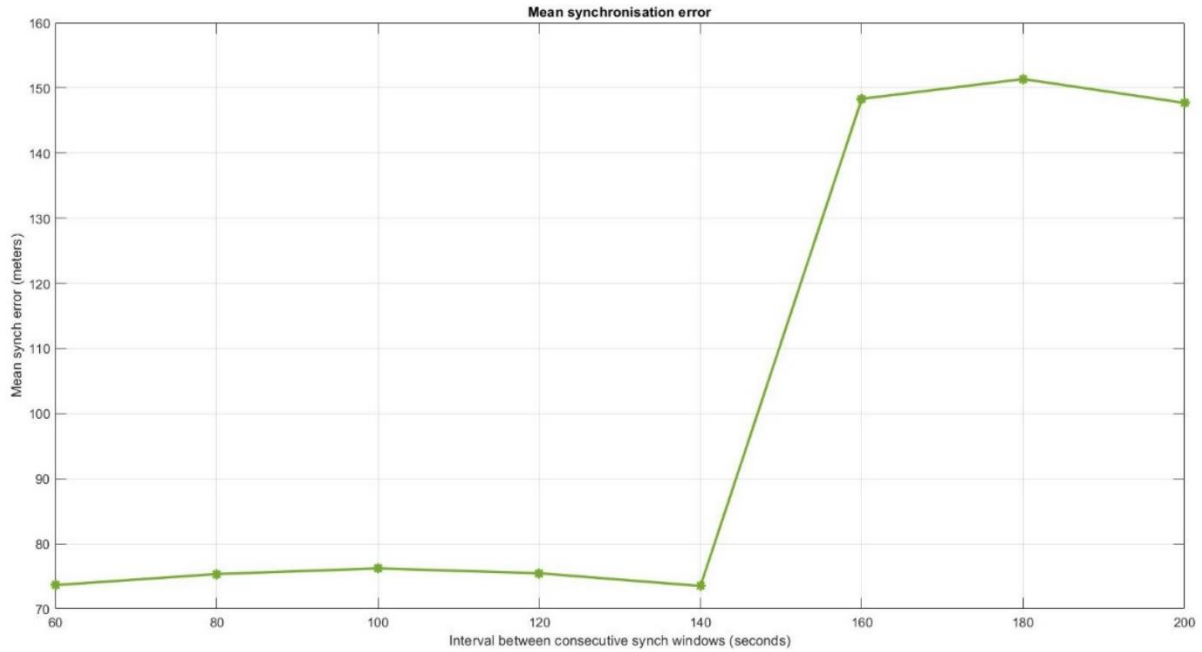
Figure 23. Mean synchronisation error expressed in meters, with $fs = 10^6$.

Finally, in the following Figures we can see the synchronisation error, both in terms of seconds and meters, but with a higher sampling frequency equal to $f_s = 10^8$. The results improve a lot (up to 10^{-9} seconds) and this is due to the fact that we reduce the duration of each sample time and, thus, we reduce the error related to the conversion from the non-integer value of the total delay to a fixed number of samples operated by the MATLAB function **`delayseq()`**. With the purpose of accelerating the computation process, the number of simulations is reduced to only some tens, since they result to be enough to have an idea of the final evolution of the error itself.
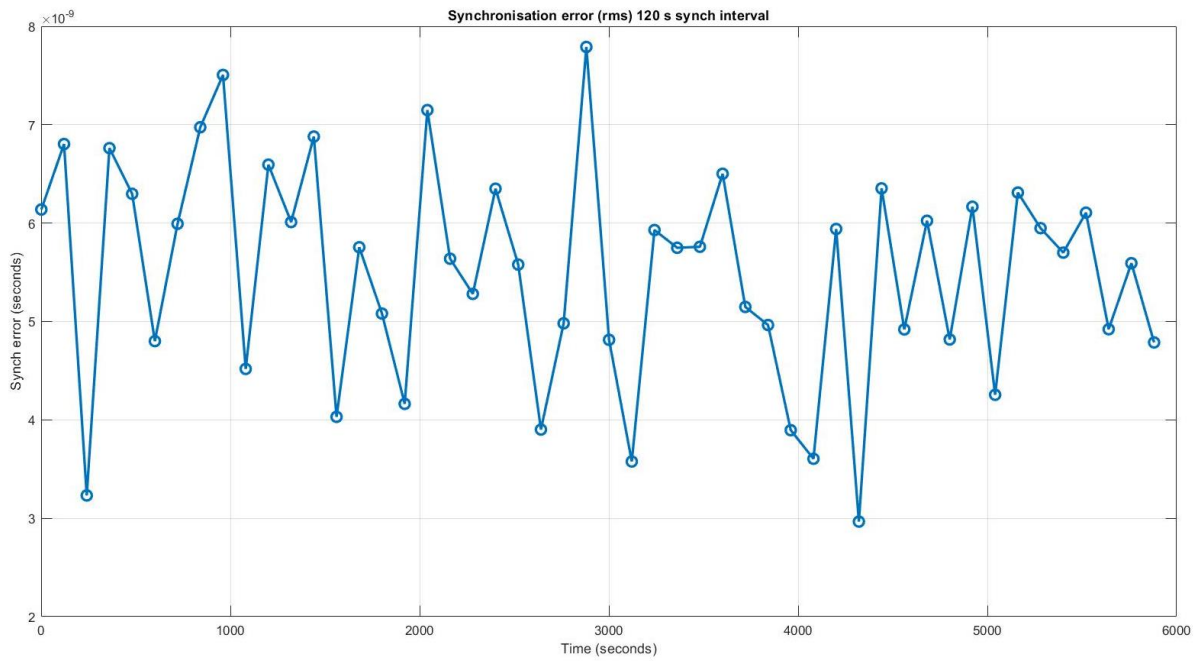
Figure 24. Synchronisation error expressed in seconds as a function of time, with $dt = 120\ s$ and $fs = 10^8$.
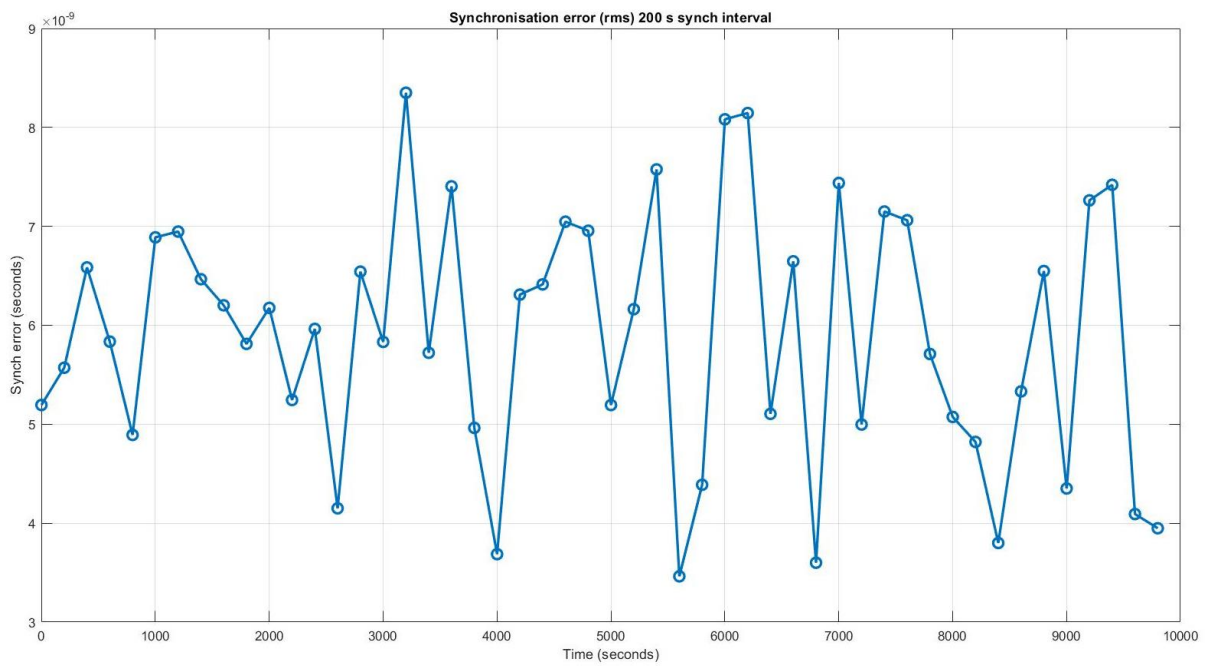
Figure 25. Synchronisation error expressed in seconds as a function of time, with $dt = 200\ s$ and $fs = 10^8$.
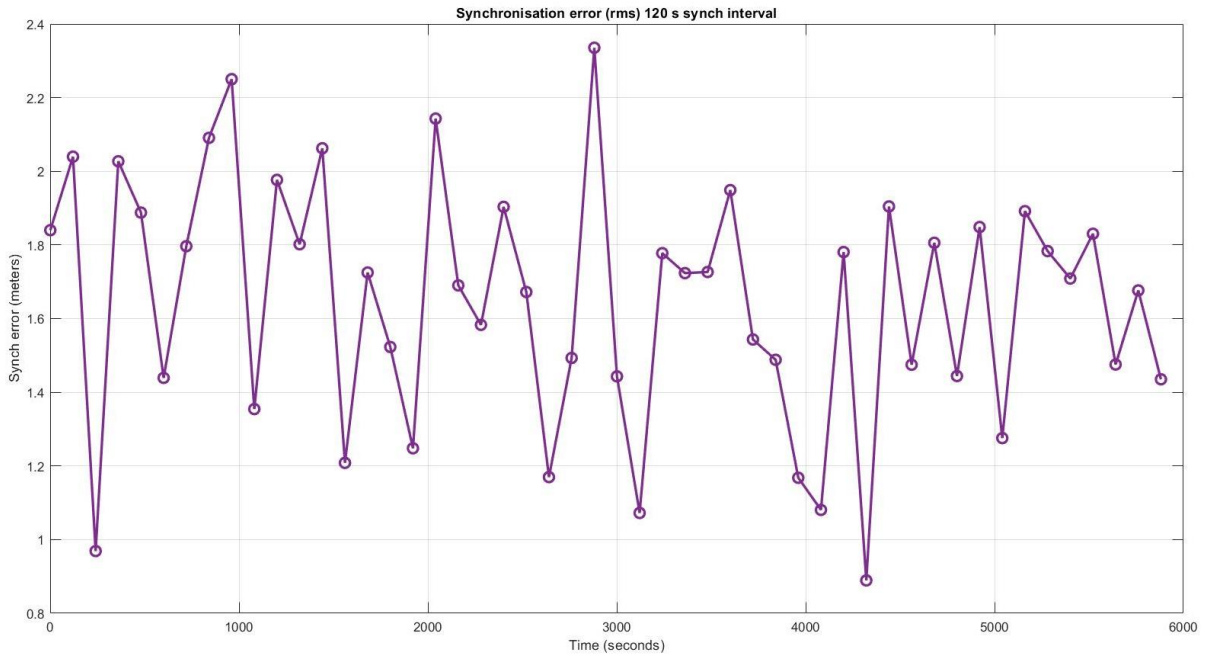
Figure 26. Synchronisation error expressed in meters as a function of time, with $dt = 120\ s$ and $fs = 10^8$
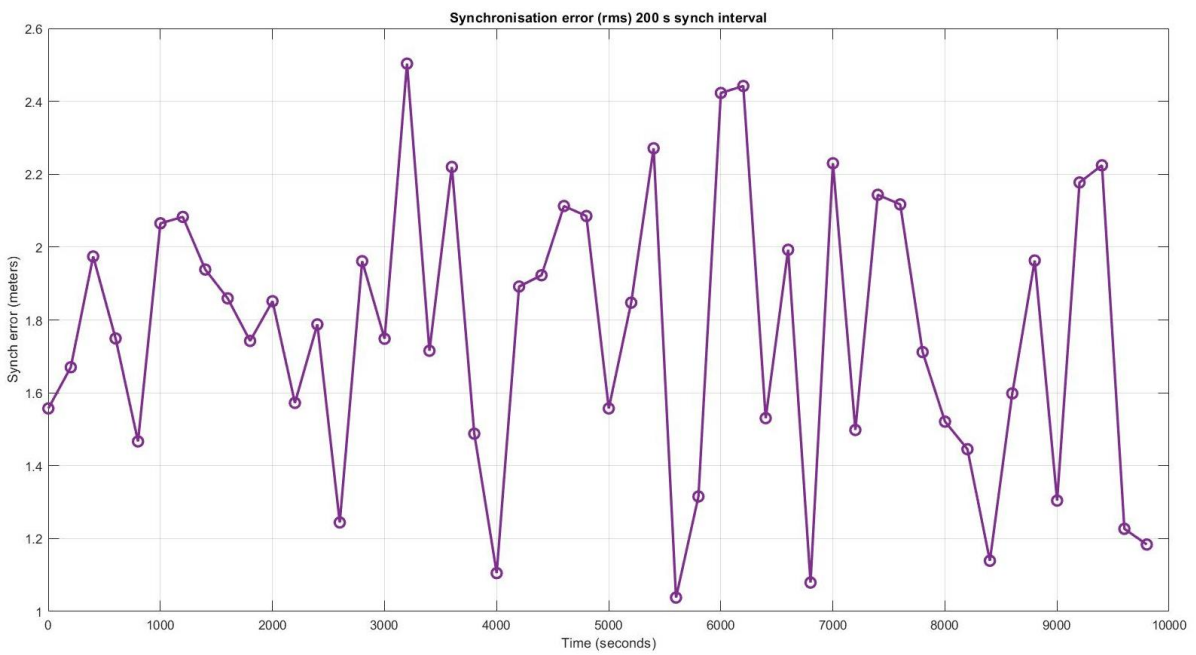
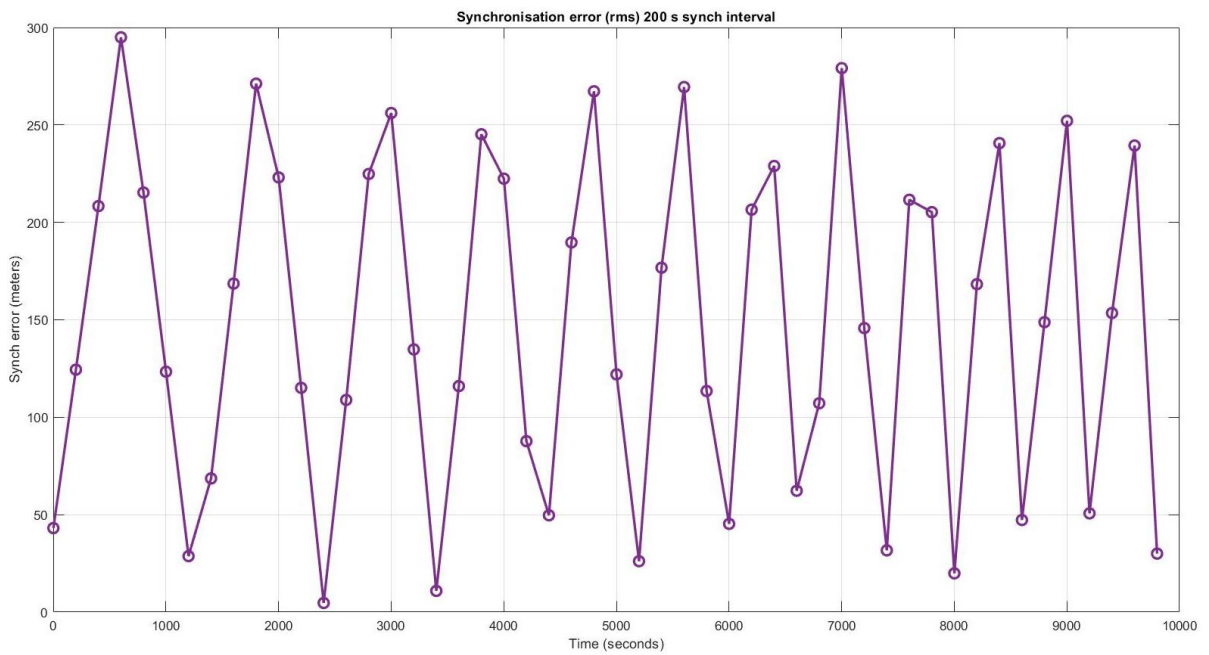*Figure 27. Synchronisation error expressed in meters as a function of time, with $dt = 200\ s$ and $fs = 10^8$.*

Conclusions and Future Works

In the first chapter of this thesis, we dealt with the importance of spacecraft navigation in the context of space exploration missions, involving the determination of the spacecraft's position and its maintenance on the desired trajectory towards a specific destination. At present, most of space missions are based on two-way range and Doppler observables, measured starting from the time taken by a radio signal to complete its round trip from the ground station to the spacecraft. However, as the spacecraft moves away from Earth, there is an increase in the propagation time of the two-way signal, making this type of navigation inadequate for all those occasions in which timely decisions are required. In this sense, we had an overview on the NASA's Deep Space Atomic Clock technological demonstration, an ultra-precise, mercury-ion atomic clock encased in a small box which has made it possible to reliably and accurately collect one-way radiometric observables sent from a ground antenna or another spacecraft.

In the second chapter, we conducted an initial study on the possibility of autonomous spacecraft navigation using one-way range and Doppler observables through a microwave link between the ground station and the spacecraft. The study involved analysing the mathematical model of the ACES mission and developing a new theoretical framework to support a novel one-way uplink architecture. To achieve this, we created a simplified model of the architecture using MATLAB programming language to obtain preliminary results and determine the practicality of this method of navigation. Specifically, we tested the feasibility of a time transfer link between an ultra-precise clock on the ground and the spacecraft clock, which had a lower temporal and frequency stability. Our work was based on opening clock synchronisation windows, separated by a specific time interval dt, and transmitting a signal from the ground station to the onboard clock to synchronise it. Once the two clocks are synchronised, the necessary radiometric measurements can be carried out.

In the last chapter, we plotted a series of graphs to observe the synchronisation error's evolution over time. The synchronisation error is the difference between the transmitted time reference and the final time reported by the spacecraft clock. From multiple tests conducted on the simulated scenario, we found that we need to start synchronising the spacecraft clock when it is not too far from Earth. This helps prevent the clock drift from becoming irrecoverable right away. We also noticed that increasing the value of the synchronisation window resulted in a higher synchronisation error. This is because the spacecraft clock drifts more during that period,

which makes it harder to recover the resulting desynchronisation with respect to the ground clock. This is evident in the transition from the graph corresponding to $dt = 60 \, s$ or $dt = 120 \, s$ to the graph corresponding to $dt = 200 \, s$, since the synchronisation error in seconds moves from an order of magnitude of 10^{-7} seconds to an order of magnitude of 10^{-6} seconds. Moreover, we observed the Mean Synchronisation Error, computed taking into account the RMS values which result from the entire set of simulations for each of the tested synchronisation windows. As shown by the graphs, it is possible to note an increase, yet small, of the Mean Synchronisation Error. The evident "jump" upwards is due to the "manual" correction performed in the MATLAB code, which is needed from 1000 delay samples on but it is still acceptable because all values remain in the same order of magnitude. Finally, we investigated the synchronisation error with a higher sampling frequency equal to $f_s = 10^8$. The results improve a lot (up to 10^{-9} seconds) and this is due to the fact that we reduce the duration of each sample time and, thus, we reduce the error related to the conversion from the non-integer value of the total delay to a fixed number of samples operated by MATLAB.

As anticipated at the beginning of the second chapter, this is a preliminary study on the possibility of building a one-way uplink architecture based on the use of a clock which needs to be synchronised at some point in time through the opening of a series of synchronisation windows. The aim of the simulated scheme is to test the application of the aforementioned ACES equations within our scenario and obtain proper results to examine the potential practicability of such one-way uplink navigation. This work will be further explored in the near future during my doctorate and it will prepare the ground for new studies. Many aspects must be examined in depth, starting from the correlation computation which seems to have some limits, as highlighted by the "manual" correction which is required from a delay equal to 1000 samples onward. Moreover, the next step will be substituting the correlation with the ACES ascending zero-crossings count as a method to compute the PToF on-board the spacecraft. In addition, we will introduce the atmospheric delays in the simulation, in order to fully test the dual frequency one-way uplink scheme, as well as orbit errors, following again the ACES model. Finally, in the context of one-way uplink deep space navigation, one of the objectives will be performing parametric analysis to quantify the maximum value of the synchronisation window time to meet the ranging and Doppler accuracies requirements, together with inserting the errors quantified in this work in a real orbit determination filter to accurately simulate a deep space one-way uplink navigation scenario.

Appendix

PURE SPECTRUM

Telecom Performance 5x7mm TCXO / VCTCXO T / TV Series

CONNOR WINFIELD

Description:

Connor-Winfield's Txxx and TVxxx series are 5x7mm TCXO and VCTCXO products with exceptional frequency stability and low phase noise. Through the use of analog temperature compensation, these products are capable of holding Stratum 3 level temperature stabilities of ±0.28 ppm over the commercial and industrial temperature ranges. Available in 4-pad or 10-pad surface mount footprints.

These products are designed for such applications as IEEE 1588 PTP and Synchronous Ethernet.

All models will meet ±4.6 ppm accuracies for twenty years

Features:
- Frequency Stabilities Available:
    +/-0.28 ppm (6.4 to 50 MHz) ✓STRATUM 3
    +/-0.50 ppm (6.4 to 50 MHz)
    +/-1.00 ppm or +/-2.00 ppm (6.4 to 54 MHz)
- Temperature Ranges Available:
    0 to 85°C, 0 to 70°C, -40 to 85°C or
    -20 to 70°C Packages Available:
- T - Series: 5 x 7mm - 10 Pad
- TV - Series: 5 x 7mm - 4 Pad
- 3.3 Vdc Operation
- Output Logic: LVCMOS or Clipped Sinewave
- Fixed Frequency - TCXO
- Voltage Controlled - VCTCXO
- Low Jitter <0.50 ps RMS
- Low Phase Noise
- Tri-State Enable/Disable: (T Model Series Only)
- Tape and Reel Packaging
- RoHS Compliant / Lead Free ✓RoHS

Applications:
- IEEE 1588 Applications
- Synchronous Ethernet slave clocks, ITU-T G.8262 EEC options 1 & 2
- Compliant to Stratum 3, GR-1244-CORE & GR-253-CORE
- Wireless Communications
- Small Cells
- Test and Measurement
- GPS

Standard Frequencies Available *
* 6.4, 9.72, 10, 10.24, 12.5, 12.8, 13.5, 19.2, 19.44, 20, 20.48, 25, 27, 38.88, 40 MHz
Available frequencies from the factory for small quantity orders or quick delivery.
Additional frequencies are available.

** Not all Models available at Digi-Key

Ordering Information

| TV | 5 | 0 | 4 | - 010.0M |

Type / Package TCXO / VCTCXO Series	Temperature Range	Frequency Stability	Features	Output Frequency
T = 5.0x7.0 mm 10 Pads TV = 5.0x7.0 mm 4 Pads	3 = 0 to 85 °C 5 = 0 to 70°C 6 = -40 to 85°C 7 = -20 to 70°C	0 = ±0.28 ppm 1 = ±0.50 ppm 2 = ±1.00 ppm 3 = ±2.00 ppm	2 = TCXO, LVCMOS, 3.3 Vdc 3 = TCXO, Clipped Sinewave, 3.3 Vdc 4 = VCTCXO, LVCMOS, 3.3 Vdc 5 = VCTCXO, Clipped Sinewave, 3.3 Vdc	Frequency Format -xxx.xM Min -xxx.xxxxxxM Max *Amount of numbers after the decimal point. M = MHz

Example: Part Number

TV504-010.0M = 5x7mm 4 pad package, ±0.28 ppm, 0 to 70°C, 3.3 Vdc, LVCMOS Output, VCTCXO
T715-012.8M = 5x7mm 10 pad package, ±0.50 ppm, -20 to 70°C, 3.3 Vdc, Clipped Sinewave Output, VCTCXO
T522-050.0M = 5x7mm 10 pad package, ±1.0 ppm, 0 to 70°C, 3.3 Vdc, LVCMOS Output, TCXO
TV602-010.0M = 5x7mm 4 pad package, ±0.28 ppm, -40 to 85°C, 3.3 Vdc, LVCMOS Output, TCXO

HCW RoHS COMPLIANT

Absolute Maximum Ratings

Parameter	Minimum	Nominal	Maximum	Units	Notes
Storage Temperature	-55	-	95	°C	
Supply Voltage (Vcc)	-0.5	-	6.0	Vdc	
Input Voltage	-0.5	-	Vcc + 0.5	Vdc	

Operating Specifications

Parameter	Minimum	Nominal	Maximum	Units	Notes
Output Frequency (Fo)					
Models Tx0x, TVx0x	6.4	-	50	MHz	
Models Tx1x, TVx1x	6.4	-	50	MHz	
Models Tx2x, TVx2x	6.4	-	54	MHz	
Models Tx3x, TVx3x	6.4	-	54	MHz	
Operating Temperature Range		(See Ordering Information for full part number)			
Models T3xx, TV3xx	0	-	85	°C	
Models T5xx, TV5xx	0	-	70	°C	
Models T6xx, TV6xx	-40	-	85	°C	
Models T7xx, TV7xx	-20	-	70	°C	
Frequency Calibration @ 25 °C	-1.0	-	1.0	ppm	1
Frequency Stability (See Ordering Information for full part number) Per STRATUM 3 GR-1244-CORE					
Frequency Stability ±0.28 ppm is only available in the frequency range of 6.4 to 50 MHz.					
Models Tx0x, TVx0x	-0.28	-	0.28	ppm	2
Holdover Stability	-0.32	-	0.32	ppm	3
Constant Temperature Stability	-40	-	40	ppb	Over 24 Hrs.
Frequency Stability	(See Ordering Information for full part number)				
Models Tx1x, TVx1x	-0.50	-	0.50	ppm	2
Models Tx2x, TVx2x	-1.00	-	1.00	ppm	2
Models Tx3x, TVx3x	-2.00	-	2.00	ppm	2
Frequency vs. Load Stability	-0.05	-	0.05	ppm	±5%
Frequency vs. Voltage Stability	-0.05	-	0.05	ppm	±5%
Static Temperature Hysteresis	-	-	0.40	ppm	4
Freq. shift after reflow soldering	-1.0	-	1.0	ppm	5
Long Term Stability	-1.0	-	1.0	ppm	6
Aging					
per Life (20 Years)	-3.0	-	3.0	ppm	
per Day	-40	-	40	ppb	
Total Frequency Tolerance	-4.6	-	4.6	ppm	7
Supply Voltage (Vcc)	3.135	3.30	3.465	Vdc	
Supply Current (Icc) LVCMOS	-	2.1	6.0	mA	
Clipped Sinewave	-	1.3	2.9	mA	
Jitter:					
Period Jitter	-	3.0	5.0	ps RMS	
Integrated Phase Jitter (12K to Fo/2)	-	0.3	1.0	ps RMS	8
Allan Deviation (1s)	-	1.0E-10	-		
G-sensitivity	-	-	2.0	ppb/g	
Typical SSB Phase Noise					
For Fo	10.0 MHz	25.0 MHz	50.0 MHz		
@ 10 Hz offset	-98	-90	-73	dBc/Hz	
@ 100 Hz offset	-125	-120	-103	dBc/Hz	
@ 1 KHz offset	-143	-140	-134	dBc/Hz	
@ 10 KHz offset	-151	-151	-151	dBc/Hz	
@ 100 KHz offset	-152	-152	-152	dBc/Hz	
@ 1 MHz offset	-155	-154	-154	dBc/Hz	
Start-Up Time	-	-	10	ms	

Bulletin	Tx176
Page	2 of 6
Revision	23
Date	07 Nov 2019

Control Voltage Input Characteristics

Parameter	Minimum	Nominal	Maximum	Units	Notes
Control Voltage	0.3	1.65	3.0	V	
Frequency Pullability	±10	±12	-	ppm	
Pull Slope (Vc=1.65V)	-	8.00	-	ppm/V	
Control Voltage Slope		Positive Slope			
Monotonic Linearity	-	-	5	%	
Input Impedance	100K	-	-	Ohm	
Modulation Bandwidth (3dB)	10	-	-		KHz

OE Enable /Disable Input Characteristics (Pad 8) T Series only

Parameter	Minimum	Nominal	Maximum	Units	Notes
Enable Input Voltage -(Vih)	70%Vcc	-	-	Vdc	9
Disable Input Voltage - (Vil)	-	-	30%Vcc	Vdc	9

Function	Output
Low:	Disabled (High Impedance)
High or Open:	Enabled

LVCMOS Output Characteristics

Parameter		Minimum	Nominal	Maximum	Units	Notes
Load (CL)		-	15	-	pF	10
Voltage (High)	(Voh)	90%Vcc	-	-	Vdc	
(Low)	(Vol)	-	-	10%Vcc	Vdc	
Current (High)	(Ioh)	-4	-	-	mA	
(Low)	(Iol)	-	-	4	mA	
Duty Cycle at 50% of Vcc		45	50	55	%	
Rise / Fall Time 10% to 90%		-	4	8	ns	

Clipped Sinewave Output Characteristics

Parameter	Minimum	Nominal	Maximum	Units	Notes
Load (RC)					11
Output Load Resistance	-	10K	-	Ohm	12
Output Load Capacitance	-	10	-	pF	
OutputVoltage (< 40 MHz)	1.0	1.2	-	V	pk-pk
OutputVoltage (=>40 MHz)	0.8	1.0	-	V	pk-pk
Output Impedance	-	200	-	Ohms	

Package Characteristics

Package   Hermetically sealed ceramic package with grounded metal cover

Environmental Characteristics

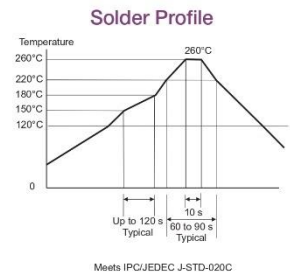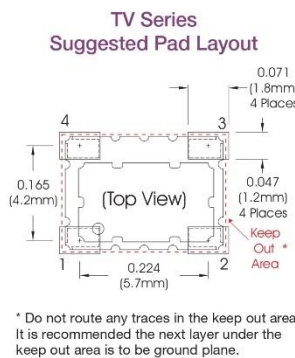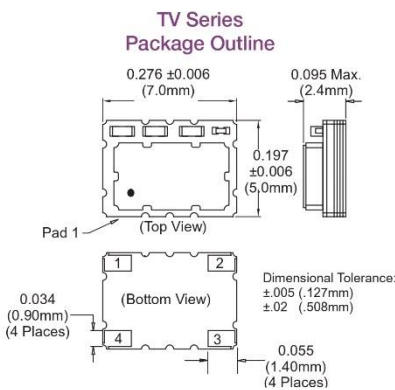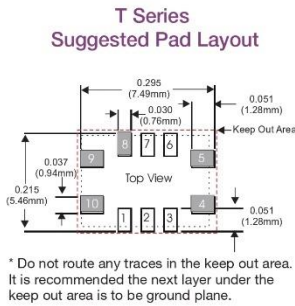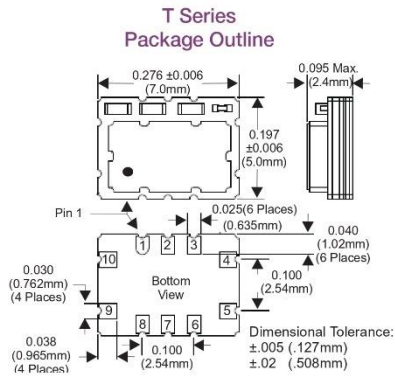Vibration: Vibration per Mil Std 883E Method 2007.3 Test Condition A.
Shock: Mechanical Shock per Mil Std 883E Method 2002.4 Test Condition B.
Soldering Process: RoHS compliant lead free. See soldering profile on page 4.

Notes:
1. Initial calibration @ 25°C. ±2°C, for VCTCXO's Vc = 1.65V. Specifications at time of shipment
2. Frequency stability vs. change in temperature. [±(Fmax-Fmin)/(2*Fo)]. For VCTCXO's - Vc -= 1.65V
3. Inclusive of frequency stability, supply voltage change (±1%), aging, for 24 hours. Per STRATUM 3 GR-1244-CORE.
4. Frequency change after reciprocal temperature ramped over the operating range. Frequency measured before and after at 25°C
5. Two consecutive solder reflows after 1 hour recovery @ 25°C.
6. Frequency drift over 1 year @ 25°C.
7. Inclusive of calibration @ 25°C, frequency vs. change in temperature, change in supply voltage (±5%), load change (±5%), reflow soldering process and 20 years aging.
8. BW = 12 KHz to 20 MHz
9. Leave Pad 8 on the T Series unconnected if enable / disable function is not required. When tri-stated, the output stage is disabled but the oscillator and compensation circuit are still active (current consumption < 1 mA).
10. Attention: To achieve optimal frequency stability, and in some cases to meet the specification stated on this data sheet, it is required that the circuit connected to this TCXO output must have the equivalent input capacitance that is specified by the nominal load capacitance. Deviations from the nominal load capacitance will have a graduated effect on the stability of approximately 20 ppb per pF load difference.
11. Load components are required for proper operation of the device.
12. Output is AC coupled.

Bulletin	Tx176
Page	3 of 6
Revision	23
Date	07 Nov 2019

T Series
Package Outline

0.276 ±0.006 (7.0mm)
0.095 Max. (2.4mm)
0.197 ±0.006 (5.0mm)

Pin 1

0.025 (6 Places) (0.635mm)
0.040 (1.02mm) (6 Places)

0.030 (0.762mm) (4 Places)

Bottom View

0.100 (2.54mm)

0.038 (0.965mm) (4 Places)

0.100 (2.54mm)

T Series
Suggested Pad Layout

0.295 (7.49mm)
0.030 (0.76mm)
0.051 (1.28mm)
Keep Out Area

0.037 (0.94mm)

Top View

0.215 (5.46mm)

0.051 (1.28mm)

* Do not route any traces in the keep out area. It is recommended the next layer under the keep out area is to be ground plane.

T Series
Pad Connections

1: Do Not Connect
2: Do Not Connect
3: Do Not Connect
4: Ground
5: Output
6: Do Not Connect
7: Do Not Connect
8: Enable / Disable (OE)
9: Supply Voltage (Vcc
10: VCTCXO: Control Voltage (Vc)
    TCXO: N/C

Dimensional Tolerance:
±.005 (.127mm)
±.02 (.508mm)

TV Series
Package Outline

0.276 ±0.006 (7.0mm)
0.095 Max. (2.4mm)
0.197 ±0.006 (5.0mm)

Pad 1

(Top View)

0.034 (0.90mm) (4 Places)

(Bottom View)

Dimensional Tolerance:
±.005 (.127mm)
±.02 (.508mm)

0.055 (1.40mm) (4 Places)

TV Series
Suggested Pad Layout

0.071 (1.8mm) 4 Places

0.165 (4.2mm)

(Top View)

0.047 (1.2mm) 4 Places
Keep Out * Area

0.224 (5.7mm)

* Do not route any traces in the keep out area. It is recommended the next layer under the keep out area is to be ground plane.

TV Series
Pad Connections

1: VCTCXO: Voltage Control (Vc)
   TCXO: N/C
2: Ground
3: Output
4: Supply (Vcc)

Solder Profile

Temperature
260°C
220°C
180°C
150°C
120°C
0

260°C
10 s

Up to 120 s Typical
60 to 90 s Typical

Meets IPC/JEDEC J-STD-020C

Marking Information

The following are examples of possible marking configurations

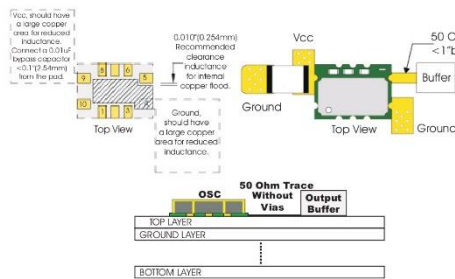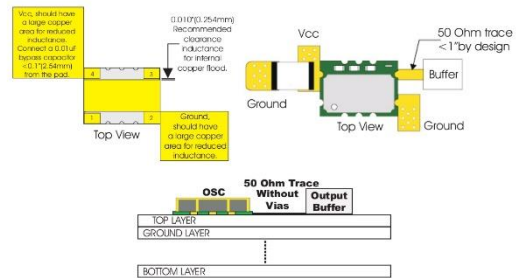*The marking varies with design configuration. All marking configurations below are valid.*

Part Number — XXXXXX YYWW — Date Code (YYWW)
XX.XXX MHZ — Frequency
XXX' XXXX — Crystal Lot Code

Part Number — XXXXXX YYWW — Date Code (YYWW)
Frequency — XXXXXXXMHZ
CW XX.XXX — Crystal Lot Code
XXX' XXXX
PIN 1

Part Number — XXXXX YM
Frequency
Date Code (YM)

Part Number — XXXXX YYWW — Date Code (YYWW)
XX.XXX MHZ — Frequency

Part Number — XXXXX YYWW — Date Code (YYWW)
XX.XXXX — Frequency
PIN 1
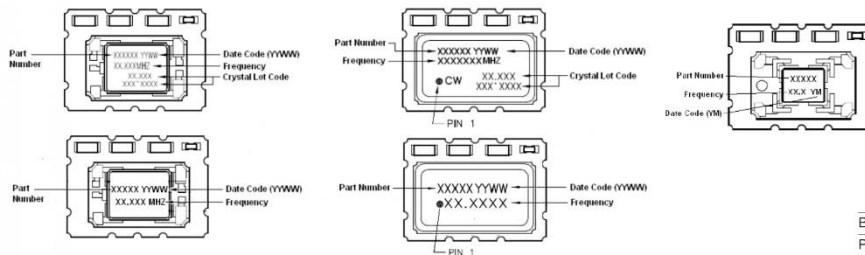
2 CHARACTER DATE CODE	
Y = Year	M = Month
8 = 2018	A = January
9 = 2019	B = February
0 = 2020	C = March
1 = 2021	D = April
	E = May
	F = June
	G = July
	H = August
	J = September
	K = October
	M = November
	N = December

Bulletin	Tx176
Page	4 of 6
Revision	23
Date	07 Nov 2019

T Series Design Recommendations

Vcc, should have a large copper area for reduced inductance. Connect a 0.01uF bypass capacitor <0.1"(2.54mm) from the pad.

0.010"(0.254mm) Recommended clearance inductance for internal copper flood.

Ground, should have a large copper area for reduced inductance.

Top View

Vcc

Ground

50 Ohm trace <1"by design

Buffer

Top View

Ground

OSC

50 Ohm Trace Without Vias

Output Buffer

TOP LAYER
GROUND LAYER

BOTTOM LAYER

TV Series Design Recommendations

Vcc, should have a large copper area for reduced inductance. Connect a 0.01uF bypass capacitor <0.1"(2.54mm) from the pad.

0.010"(0.254mm) Recommended clearance inductance for internal copper flood.

Ground, should have a large copper area for reduced inductance.

Top View

Vcc

Ground

50 Ohm trace <1"by design

Buffer

Top View

Ground

OSC

50 Ohm Trace Without Vias

Output Buffer

TOP LAYER
GROUND LAYER

BOTTOM LAYER

T Series
LVCMOS Test Circuit

Enable/Disable DNC DNC

Vcc Supply Voltage

9 8 7 6 5

10 1 2 3 4 Ground

Output

TCXO = N/C
VCTCXO = Vc

DNC DNC DNC

DNC = Do Not Connect

0.1 uF Bypass

10 nF Bypass

15 pF

TV Series
LVCMOS Test Circuit

Vcc Supply Voltage

4 3

1 2 Ground

Output

TCXO = N/C
VCTCXO = Vc

0.1 uF Bypass

10 nF Bypass

15 pF

LVCMOS Output Waveform

1V/Div

T Series
Clipped Sinewave Test Circuit

Enable/Disable DNC DNC

Vcc Supply Voltage

9 8 7 6 5

10 1 2 3 4 Ground

Output

TCXO = N/C
VCTCXO = Vc

DNC DNC DNC

DNC = Do Not Connect

0.1 uF Bypass

10 nF Bypass

10 pF

10K Ohm

TV Series
Clipped Sinewave Test Circuit

Vcc Supply Voltage

4 3

1 2 Ground

Output

TCXO = N/C
VCTCXO = Vc

0.1 uF Bypass

10 nF Bypass

10 pF

10K Ohm
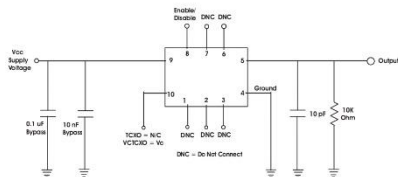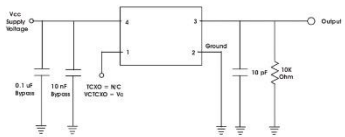
Clipped Sinewave
Output Waveform

200 mV/Div
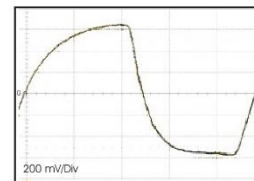
Note: The clipped sinewave output is AC coupled

Bulletin	Tx176
Page	5 of 6
Revision	23
Date	07 Nov 2019

Phase Noise Information

Model TV504-010.0MHz

TIE

TV504-010.0M: WANDER GENERATION IN A STRATUM 3 PLL AT 0.098 Hz BANDWIDTH

MTIE

TV504-010.0M: MTIE per GR-253-CORE

TDEV

TV504-010.0M: TDEV per GR-253-CORE
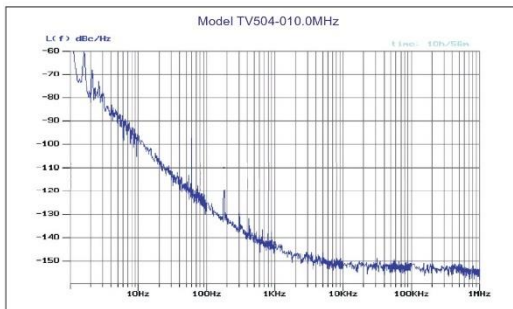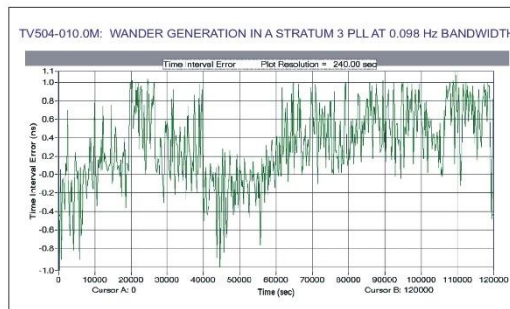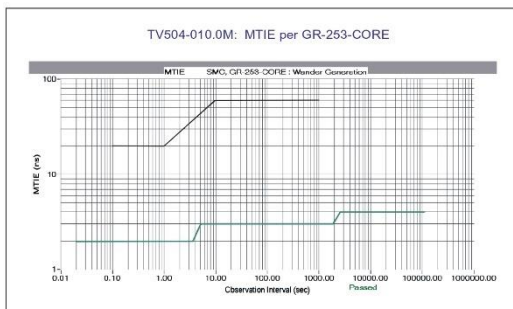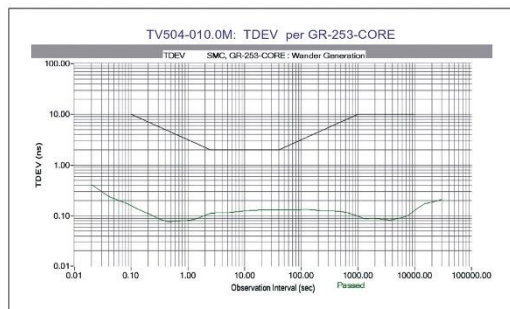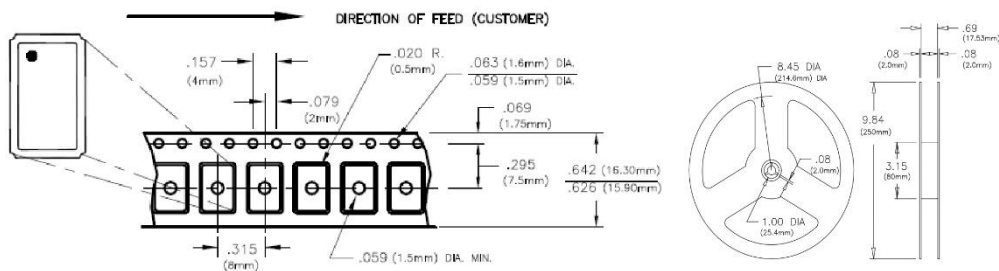
5x7mm Tape and Reel Information

MEETS EIA-481A AND EIAJ-1009B
700 PCS/REEL MAXIMUM.

Revision History

Revision	Date	Action
19	04/01/15	Updated Frequency Stabilities
20	07/27/16	Extended operating frequency range, and updated standard frequency list
21	05/10/17	Added marking variations
22	08/02/18	Height change to 2.4mm Max and added additional marking variation
23	11/07/19	Added G-sensitivity specfication.

Bulletin	Tx176
Page	6 of 6
Revision	23
Date	07 Nov 2019

Bibliography

- Allan D. W., "Statistics of atomic frequency standards", Proceedings of the IEEE, vol. 54, no. 2, 1966, pp. 221-230, doi: 10.1109/PROC.1966.4634.

- Angonin M.C., Delva P., Guerlin C., Lilley M., Savalle E. et al., "ACES/PHARAO: high-performance space-to-ground and ground-to-ground clock comparison for fundamental physics", GPS Solutions, 25 (2), 2021, doi: 10.1007/s10291-020-01058-y.

- Baron P., Hobiger T., Piester D., "A correction model of dispersive troposphere delays for the ACES microwave link", Radio Science, vol. 48, no. 2, 2013, pp. 131-142, doi: 10.1002/rds.20016.

- Bian L., Lei W., Meng Y., Wang G., Wang Y., Yan T., "One-way deep space navigation with radiometric and inertial data fusion", 2017 20th International Conference on Information Fusion (Fusion), Xi'an, China, 2017, pp. 1-5, doi: 10.23919/ICIF.2017.8009715.

- Border J. S., Thornton C. L., "Radiometric Tracking Techniques for Deep-Space Navigation", JPL Publication, 2000.

- Cacciapuoti L., Laurent P., Massonnet D., Salomon C., "The ACES/PHARAO space mission", Comptes-Rendus Acad. Sciences, Paris, Volume 16, Issue 5, 2015, pp. 540-552, doi: 10.1016/j.crhy.2015.05.002.

- Cacciapuoti L., Salomon C., "Space clocks and fundamental tests: The ACES experiment", The European Physical Journal - Special Topics, 172, 57–68, 2009, doi: 10.1140/epjst/e2009-01041-7.

- Delva P., Laurent P., Le Poncin-Lafitte C., Meynadier F., Wolf P., "Time and frequency transfer with a MicroWave Link in the ACES/PHARAO mission," 2012 European Frequency and Time Forum, Gothenburg, Sweden, 2012, pp. 28-35, doi: 10.1109/EFTF.2012.6502327.

- Duchayne L., "Transfert de temps de haute performance: le Lien Micro-Onde de la mission ACES", Physique mathématique [math-ph], Observatoire de Paris, 2008, Français.

- Duchayne L., Mercier F., Wolf P., "Orbit determination for next generation space clocks", Astronomy and Astrophysics, vol. 504, 2009, pp. 653–661, doi: 10.1051/0004-6361/200809613.

- Ely T. et al., "Deep Space Atomic Clock Technology Demonstration Mission Results", 2022 IEEE Aerospace Conference (AERO), Big Sky, MT, USA, 2022, pp. 1-20, doi: 10.1109/AERO53065.2022.9843303.

- Ely T., Seubert J., "One-Way Radiometric Navigation with the Deep Space Atomic Clock", 2015 AAS/AIAA Space Flight Mechanics Meeting, Williamsburg, VA, USA, 2015.

- Laurent P. et al., "Design of the cold atom PHARAO space clock and initial test results", Applied Physics B - Laser and Optics, 84, 2006, pp. 683-690, doi: 10.1007/s00340-006-2396-6.

- Meynadier F. et al., "Atomic Clock Ensemble in Space (ACES) data analysis", Classical and Quantum Gravity, Volume 35, Number 3, 2018, doi: 10.1088/1361-6382/aaa279.

- NASA/JPL, "Deep Space Atomic Clock – NASA Facts", JPL Publication, 2013.

- Riley W., "Handbook of Frequency Stability Analysis", Special Publication (NIST SP), National Institute of Standards and Technology, Gaithersburg, MD, 2008, [online], https://tsapps.nist.gov/publication/get_pdf.cfm?pub_id=50505 (Accessed October 2, 2023).

- Saastamoinen J., "Contribution to the Theory of Atmospheric Refraction", Bulletin Géodésique, 107, 1973, pp. 13-34, doi: 10.1007/BF02522083.

- Will C.M., "The Confrontation between General Relativity and Experiment", Living Rev. Relativ. 17, 4, 2014, doi: 10.12942/lrr-2014-4.

Sitography

- ACES Workshop, Paris, France, 2022, SciencesConf website, <https://aces2022.sciencesconf.org/>, accessed on 31st August 2023.

- "Challenges of Space Navigation", <https://timeandnavigation.si.edu/navigating-space/challenges>, accessed on 3rd August 2023.

- Cofield C., "Deep Space Atomic Clock Moves Toward Increased Spacecraft Autonomy", 2021, NASA website, <https://www.nasa.gov/feature/jpl/deep-space-atomic-clock-moves-toward-increased-spacecraft-autonomy>, accessed on 4th September 2023.

- Doody D., "Basics of Space Flight - Chapter 13: Navigation", 2022, Solar System Exploration: NASA Science website, <https://solarsystem.nasa.gov/basics/chapter13-1/>, accessed on 12th July 2023.

- O'Neill I. J., "Working Overtime: NASA's Deep Space Atomic Clock Completes Mission", 2021, Jet Propulsion Laboratory website, <https://www.jpl.nasa.gov/news/working-overtime-nasas-deep-space-atomic-clock-completes-mission>, accessed on 31st August 2023.

- Sarang M., Weinzierl M., "The Commercial Space Age Is Here", 2021, Harvard Business Review website, <https://hbr.org/2021/02/the-commercial-space-age-is-here>, accessed on 3rd August 2023.

Ringraziamenti / Acknowledgements

L'umanità è stata sempre attratta dall'ignoto, dalla voglia di conoscere cosa si trova dietro l'angolo, dalla insaziabile spinta a voler rispondere alle grandi domande della vita, individuali e collettive: chi sono io? Qual è il mio scopo? Come sarà il mondo tra dieci anni o a distanza di un secolo intero? Cosa si cela nella vastità del cosmo? Questa vorace curiosità ha permesso all'umanità di spostare le colonne d'Ercole della conoscenza ogni volta un passo più in là, accompagnando la nostra storia e la nostra evoluzione in quanto specie. Ho sempre cercato di coltivare questa curiosità, questa voglia di conoscere, facendone una guida nello studio ma, soprattutto, nella vita e se oggi posso celebrare questo traguardo è proprio dovuto ad essa e a tutte le persone che l'hanno ispirata durante il percorso.

Devo ringraziare innanzitutto il professor Marco Zannoni, relatore di questa tesi, il professor Paolo Tortora e il dottor Edoardo Gramigna, correlatori, i quali mi hanno fornito la guida, l'esperienza e il supporto necessari per poter dare vita a questo lavoro.

Voglio ringraziare dal più profondo del cuore la mia ragazza, la quale ha sempre creduto in me e mi ha permesso di credere in me anche nei momenti più difficili, donandomi sostegno, conforto, fiducia e ispirandomi a guardare sempre al domani.

Un ringraziamento sincero ai miei amici pavolosi, Nicolò, Christian, Gianmarco, Cecilia, Giulia, Saba, Vittoria e Katharina, per avermi regalato sorrisi e spensieratezza e per rappresentare un punto fermo nella mia vita.

Voglio poi ringraziare tutta la mia famiglia per aver sostenuto la mia crescita personale e per avermi accompagnato in ogni passo di questo percorso. Un ringraziamento particolare a mia madre e a mia nonna per avermi sempre permesso di scegliere liberamente, per avermi insegnato a rialzarmi dopo ogni inciampo e a non aver mai paura di mostrarmi per quello che sono.

Infine, voglio ringraziare la persona che è stata sempre il mio punto di riferimento, mio nonno, il quale ha acceso in me la fiamma della curiosità e mi ha insegnato che, per quanti colpi possa infliggere la vita, dobbiamo viverla all'insegna dell'amore, della generosità e della conoscenza, proprio come lui ha fatto.